


The MURALEs survey

VI. Properties and origin of the extended line emission structures in radio galaxies

B. Balmaverde¹, A. Capetti¹, R. D. Baldi², S. Baum³, M. Chiaberge^{4,5}, R. Gilli⁶, A. Jimenez-Gallardo^{7,1,8,9}, A. Marconi^{10,11}, F. Massaro^{7,1,9}, E. Meyer¹², C. O’Dea³, G. Speranza^{13,14}, E. Torresi⁶, and G. Venturi^{15,11}

¹ INAF – Osservatorio Astrofisico di Torino, Via Osservatorio 20, 10025 Pino Torinese, Italy
e-mail: barbara.balmaverde@inaf.it

² INAF – Istituto di Radioastronomia, Via Gobetti 101, 40129 Bologna, Italy

³ Department of Physics and Astronomy, University of Manitoba, Winnipeg, MB R3T 2N2, Canada

⁴ Space Telescope Science Institute, 3700 San Martin Dr., Baltimore, MD 21210, USA

⁵ Johns Hopkins University, 3400 N. Charles Street, Baltimore, MD 21218, USA

⁶ INAF – Osservatorio di Astrofisica e Scienza dello Spazio di Bologna, Via Gobetti 93/3, 40129 Bologna, Italy

⁷ Dipartimento di Fisica, Università degli Studi di Torino, Via Pietro Giuria 1, 10125 Torino, Italy

⁸ European Southern Observatory, Alonso de Córdova 3107, Vitacura, Región Metropolitana, Chile

⁹ Istituto Nazionale di Fisica Nucleare, Sezione di Torino, 10125 Torino, Italy

¹⁰ Dipartimento di Fisica e Astronomia, Università di Firenze, Via G. Sansone 1, 50019 Sesto Fiorentino, Firenze, Italy

¹¹ INAF – Osservatorio Astrofisico di Arcetri, Largo Enrico Fermi 5, 50125 Firenze, Italy

¹² University of Maryland Baltimore County, 1000 Hilltop Circle, Baltimore, MD 21250, USA

¹³ Instituto de Astrofísica de Canarias, Calle Via Láctea, s/n, 38205 La Laguna, Tenerife, Spain

¹⁴ Departamento de Astrofísica, Universidad de La Laguna, 38206 La Laguna, Tenerife, Spain

¹⁵ Instituto de Astrofísica, Facultad de Física, Pontificia Universidad Católica de Chile, Casilla 306, Santiago 22, Chile

Received 3 December 2021 / Accepted 14 March 2022

ABSTRACT

This is the sixth paper presenting the results of the MUse RAdio Loud Emission line Snapshot survey. We observed 37 radio sources from the 3C sample with $z < 0.3$ and a declination $< 20^\circ$ with the Multi Unit Spectroscopic Explorer optical integral field spectrograph at the Very Large Telescope. Here, we focus on the properties of the extended emission line regions (EELRs) that can be studied with unprecedented detail thanks to the depth of these observations. Line emission in the ten FR IIs is, in most cases, confined to within $\lesssim 4$ kpc, while large-scale ($\gtrsim 4$ kpc) ionized gas is seen in all but two of the 26 FR IIs. It usually takes the form of elongated or filamentary structures, typically extending between 10 and 30 kpc, but also reaching distances of ~ 80 kpc. We find that the large-scale ionized gas structures show a tendency to be oriented at large angles from the radio axis, and that the gas on a scale of a few kiloparsecs from the nucleus often shows ordered rotation with a kinematical axis forming a median angle of 65° with the radio axis. We also discuss the velocity field and ionization properties of the EELRs. The observed emission line structures appear to be associated with gaseous “superdisks” that formed after a gas-rich merger. The different properties of the EELR can be explained with a combination of the source evolutionary state and the orientation of the superdisk with respect to the radio axis. The general alignment between the superdisks and radio axis might be produced by stable and coherent accretion maintained over long timescales.

Key words. galaxies: active – galaxies: ISM – galaxies: jets

1. Introduction

Radio galaxies (RGs) are among the most energetic manifestations of active galactic nuclei (AGNs) and harbor the most supermassive black holes (SMBHs) in the Universe, typically hosted in the brightest galaxies at the center of clusters or groups. They are therefore extraordinarily relevant when addressing important unknowns relating the interaction between SMBHs to their environment. It is in fact becoming increasingly clear that feedback from AGNs, that is the exchange of energy and matter between the active nucleus and the surrounding medium, is a fundamental ingredient in the formation and evolution of large-scale astrophysical structures and for the luminosity function of galaxies (see, e.g., Fabian 2012).

The evidence of kinetic AGN feedback is often witnessed in local radio galaxies, for example from the presence of cavities inflated by the radio emitting gas seen in the X-ray images (e.g., Bîrzan et al. 2004; McNamara & Nulsen 2012). However, we still lack a comprehensive view of the effects that highly collimated jets and nuclear emission have on the host and its immediate environment. In particular, questions remain about the coupling between radio outflows and ionized gas, and whether the AGN outflows enhance or quench star formation (positive or negative feedback, e.g., Camiani et al. 2016) and under which conditions.

In jetted AGNs, the study of the properties of ionized gas represents a powerful tool to explore AGN feedback. Although warm gas is a relatively minor constituent of the interstellar

medium (ISM), the optical emission lines that it produces provide us with several key diagnostics, as it enables us to study its kinematics, measure physical quantities (such as density and mass), and to identify its ionization mechanism.

Large-scale structures of optical line-emitting gas have been observed around quasistellar objects (QSOs) since the 1970s (Wampler et al. 1975; Stockton 1976; Richstone & Oke 1977). Follow-up surveys of low-redshift QSOs ($z < 0.45$) showed that optical extended emission is mostly found around steep-spectrum radio-loud quasars (Stockton & MacKenty 1983, 1987). In some cases, the ionized gas is distributed in complex filaments, which is apparently unrelated to the stars in the host galaxy or the radio structure (Stockton et al. 2002, 2006). Stockton & MacKenty (1987) noted that the presence of close companion galaxies or a disturbed morphology in optical images suggests that the extended ionized gas could be associated with tidal debris resulting from interactions or mergers. The origin of the gas and the physical mechanism that produces the distribution and the ionization properties of the gas in the extended emission line regions (EELRs) are still uncertain.

Chambers et al. (1987) and McCarthy et al. (1987) first demonstrated that the stellar continuum and the emission lines are both aligned along the radio axis in sources at a redshift ≥ 0.6 . A tendency for a spatial relationship between the gas in the EELRs and the radio source, in both radio galaxies and radio-loud, steep-spectrum quasars in lower redshift objects ($z < 0.6$) was also found by Baum & Heckman (1989a). In these sources, the extent of the radio source is similar to or greater than the extent of the emission-line gas. These authors pointed out that large Fanaroff & Riley (1974) type II (FR II) radio sources (>150 kpc) show the brightest emission line features along an axis that is skewed relative to the radio source axis and they detected emission-line filaments perpendicular to the radio structure in several sources. McCarthy & van Breugel (1989) demonstrated that the degree of alignment increases with redshift.

The primary mechanisms for the emission-line gas alignment are thought to be shocks induced by the radio jets and photoionization from the central AGN (e.g., Baum & Heckman 1989b; Baum et al. 1992; McCarthy 1993; Best et al. 2000). Tadhunter et al. (1998) suggested that the density of emitting line clouds is enhanced at higher redshift because of the compression effect of shocks driven through the ISM by the radio jets becomes increasingly important as the redshift and radio power increase. Therefore, the alignment depends on both the presence of extended gas in the environment as well as the ability of the radio source to influence its environment (see also Inskip et al. 2002, 2005). There are a few examples of emission-line gas at low z in which bright compact emitting line regions are cospatial to radio jets or radio knots (e.g., Stockton & MacKenty 1987; Tadhunter et al. 2000).

Significant progress in understanding the fueling and evolution of the activity of radio-loud AGNs, the triggering process of the radio emission, and its impact on the environment has been made studying the third Cambridge catalog of RGs (Laing et al. 1983; Spinrad et al. 1985). The 3C catalog is the premiere statistically complete sample of powerful RGs selected at 178 MHz with a flux density limit of 9 Jy; it covers a large range of radio power, it contains all types of RGs from the point of view of their optical spectrum, radio morphology, and environment. In the last two decades, a superb suite of ground- and space-based observations at all accessible wavelengths has been built with all major observing facilities from *Hubble* Space Telescope (with images from the ultraviolet to the near-infrared and also includ-

ing emission line imaging), to *Chandra*, *Spitzer*, *Herschel*, Very Large Array, as well as ground-based optical spectra.

Privon et al. (2008) and Baldi et al. (2019) presented HST narrow-band emission-line images of a large sample of 3CR radio sources. Privon et al. (2008) confirmed a weak alignment at low redshift ($z < 0.6$) between the radio and optical emission line structures and suggested that both mechanical and radiant energy are responsible for this alignment. The dominant mechanism responsible for the emission line is photoionization by nuclear radiation, but the relation between the line emission, radio, and X-ray luminosities indicates that the kinetic energy deposited in the EELRs by the jets has an important contribution.

The advent of the Multi Unit Spectroscopic Explorer (MUSE), the wide field integral field unit mounted at the Very Large Telescope, enables us to explore the emission line properties with unprecedented detail. An example of the capabilities of MUSE to study the properties of the EELRs and AGN feedback comes from the data obtained in a pilot study for 3C 317 (Balmaverde et al. 2018). In this source, a network of line filaments enshrouds the northern cavity indicating that the radio jets strongly affect the gas clouds in the surrounding medium: they displace a large amount of hot gas and filaments of line-emitting gas. The gas kinematics show the hallmarks of a shell expansion, with both blue- and red-shifted regions, with a velocity of ~ 250 km s $^{-1}$.

As part of the MUSE Radio Loud Emission line Snapshot (MURALES) survey, we observed a sample of 37 RGs with MUSE. The sample includes the 3C radio sources limited to $z < 0.3$ and $\delta < 20^\circ$. The main aim of this survey is to obtain deep emission line images and explore the gas properties in the EELRs and their relationship with the relativistic outflows. This enables us to explore the effects of feedback in radio-loud AGNs. In Balmaverde et al. (2019, 2021), we presented the main results of these observations. Thanks to their unprecedented depth (the median 3σ surface brightness limit in the emission line maps is 6×10^{-18} erg s $^{-1}$ cm $^{-2}$ arcsec $^{-2}$), these observations reveal emission line structures extending to several tens of kiloparsec in most objects.

In Speranza et al. (2021), we looked for outflow from the sources by analyzing the emission line profiles of the 37 MURALES sources. We found evidence of nuclear outflows in 21 sources, with velocities between ~ 400 and 1000 km s $^{-1}$, while extended outflows were found in 13 sources, with sizes between 0.4 and 20 kpc. Comparing the jet power, the AGN nuclear luminosity, and the outflow kinetic energy rate, we concluded that outflows of high excitation galaxies (HEGs) are likely radiatively powered, while jets likely play a role only in low excitation galaxies (LEGs). Given the gas masses, velocities, and energetics involved, the observed ionized outflows have a limited impact on the gas content or the star formation in the host.

Here we present the analysis of the properties of the EELRs and of their relationship with the radio outflows. The paper is organized as follows: in Sect. 2 we study the geometry and kinematics of the ionized gas, while in Sects. 3 and 4 we explore the connection between radio and the EELR. In Sect. 5 we discuss the ionization properties of the EELR. The results are discussed in Sect. 6 and summarized in Sect. 7.

We adopt the following set of cosmological parameters: $H_0 = 69.7$ km s $^{-1}$ Mpc $^{-1}$ and $\Omega_m = 0.286$ (Bennett et al. 2014). We use cgs units throughout the whole paper unless stated otherwise.

Table 1. Sample properties.

| Name | Redshift | FR | Exc. class | Radio | | Line emission | | | Kinemetry PA | Host PA | |
|----------|----------|----|---------------|-------|------|---------------|--------|-----------|-----------------|------------|-----|
| | | | | PA | LAS | PA (1) | PA (2) | r (kpc) | | | |
| 3C 015 | 0.073 | I | LEG | 152 | 59 | [N II] | 120 | 0 | 6.7 | – | 20 |
| 3C 017 | 0.220 | II | BLO | 156 | 49 | [N II] | 280 | | 11.6 | – | 0 |
| 3C 018 | 0.188 | II | BLO | 163 | 167 | [O III] | 50 | 270 | 20.1 | – | 165 |
| 3C 029 | 0.045 | I | LEG | 160 | 115 | [O III] | | | | – | 100 |
| 3C 033 | 0.060 | II | HEG | 19 | 313 | [O III] | 70 | 270 | 10.7 | 80 | 165 |
| 3C 040 | 0.018 | I | LEG | 13 | 450 | [N II] | | | | – | 100 |
| 3C 063 | 0.175 | II | HEG | 33 | 53 | H α | 260 | 90 | 31.5 | – | 75 |
| 3C 076.1 | 0.032 | I | – | 130 | 106 | [N II] | 50 | 270 | 4.2 | 110 | 130 |
| 3C 078 | 0.028 | I | LEG | 53 | 39 | [N II] | | | | 80 | 155 |
| 3C 079 | 0.256 | II | HEG | 105 | 537 | [O III] | 160 | 330 | 35.7 | 0 | 15 |
| 3C 088 | 0.030 | II | LEG | 55 | 107 | [N II] | 90 | | 3.7 | 120 | 150 |
| 3C 089 | 0.138 | I | – | 120 | 161 | [N II] | 300 | | 8.8 | – | 40 |
| 3C 098 | 0.030 | II | HEG | 25 | 145 | [O III] | 350 | 170 | 16.3 | 5 | 55 |
| 3C 105 | 0.089 | II | HEG | 127 | 131 | [O III] | | | | 10 | 50 |
| 3C 135 | 0.125 | II | HEG | 75 | 216 | [O III] | 230 | 50 | 43.7 | 30 | 130 |
| 3C 180 | 0.220 | II | HEG | 10 | 3080 | [O III] | 40 | 210 | 34.9 | 35 | 30 |
| 3C 196.1 | 0.198 | II | LEG | 45 | 63 | [O III] | 60 | | 14.5 | – | 50 |
| 3C 198 | 0.081 | II | SF | 30 | 117 | H α | 220 | | 35.2 | 0 | 65 |
| 3C 227 | 0.086 | II | BLO | 85 | 514 | [O III] | 50 | 220 | 49.6 | 120 | 0 |
| 3C 264 | 0.021 | I | LEG | 120 | 68 | [N II] | | | | 145 | 15 |
| 3C 272.1 | 0.003 | I | LEG | 175 | 5 | [N II] | 80 | 260 | 0.5 | 80 | 130 |
| 3C 287.1 | 0.216 | II | BLO | 90 | 283 | [O III] | 170 | 40 | 27.0 | 100 | 30 |
| 3C 296 | 0.024 | I | LEG | 35 | 130 | [N II] | | | | – | 145 |
| 3C 300 | 0.270 | II | HEG | 132 | 374 | [O III] | 130 | 260 | 36.3 | 85 | 125 |
| 3C 318.1 | 0.045 | – | – | | | [N II] | 190 | | 18.1 | – | 105 |
| 3C 327 | 0.105 | II | HEG | 100 | 489 | [N II] | 170 | 20 | 16.3 | 45 | 135 |
| 3C 348 | 0.155 | I | ELEG | 36 | 545 | H α | 280 | 110 | 28.2 | 0 | 145 |
| 3C 353 | 0.030 | II | LEG | 82 | 125 | H α | 0 | 180 | 15.4 | – | 75 |
| 3C 386 | 0.017 | II | – | 16 | 88 | [N II] | 80 | 270 | 10.1 | 130 | 105 |
| 3C 403 | 0.059 | II | HEG | 86 | 110 | [O III] | 200 | 30 | 8.7 | 35 | 40 |
| 3C 403.1 | 0.055 | II | LEG | 127 | 260 | H α | 230 | 50 | 5.3 | 20 | 150 |
| 3C 424 | 0.127 | II | LEG | 155 | 28 | [N II] | 130 | | 29.0 | 80 | 80 |
| 3C 442 | 0.026 | II | LEG | 63 | 322 | [N II] | 190 | | 4.1 | 120 | 130 |
| 3C 445 | 0.056 | II | BLO | 173 | 532 | [O III] | 235 | 105 | 15.7 | – | – |
| 3C 456 | 0.233 | II | HEG | 17 | 21 | [O III] | | | | 120 | – |
| 3C 458 | 0.289 | II | HEG | 75 | 804 | [O III] | 30 | 220 | 81.2 | 20 | 55 |
| 3C 459 | 0.220 | II | BLO | 97 | 28 | [O III] | 320 | | 59.6 | 120 | – |

Notes. Column description: (1) source name; (2) redshift; (3) and (4) radio morphological classification and excitation class from [Buttiglione et al. \(2010\)](#) (LEG = low excitation galaxy, HEG = high excitation galaxy, BLO = broad line object, SF = star-forming galaxy, ELEG = extremely low excitation galaxy); (5) and (6) position angle and largest angular size of the radio source with uncertainties usually between 5° and 10°; (7)–(9) emission line considered and position angles of the ionized gas on each side of the nucleus, (10) largest distance of emission line detection, (11) perpendicular to the line of nodes derived with the kinemetry software (kinematical axis), (12) host position angle.

2. Properties of the ionized gas

In Table 1 we list the main properties of the sample of the sources observed with MUSE, derived from the literature and from our spectroscopic data. More specifically, we provide the source redshift, its radio morphological classification and its excitation class from [Buttiglione et al. \(2010\)](#), the position angle (PA, measured anticlockwise starting from the north) and largest angular size (LAS) of the radio source¹, the PA of the ionized gas on

¹ The radio images were retrieved from the NRAO VLA Archive Survey, (c) AUI/NRAO, available at <https://data.nrao.edu/portal/#/>. For each source, we considered the map that best shows its radio structure. The radio PA was measured as the line joining the brightest emission regions on each side of the nucleus, while the LAS was measured at three times the noise level of each image.

each side of the nucleus and the largest distance of emission line detection, the perpendicular to the line of nodes derived with the kinemetry software (in the following kinematical axis, see Sect. 2.2), and the host position angle.

In Fig. 1 we present the main results obtained for one of our targets, 3C 33, as an example, and all other sources are presented in the Appendix A. In the left panel, we show the image obtained for the brightest emission line, as listed in Table 1; to this image, we superpose the orientation of the emission line structures on both sides of the nucleus (solid white lines), the orientation of the kinematical major axis in the inner regions (gray line), and the radio PA (dotted white lines). The white rectangle represents the region from which we extracted the velocity curve that is shown in the right panel.

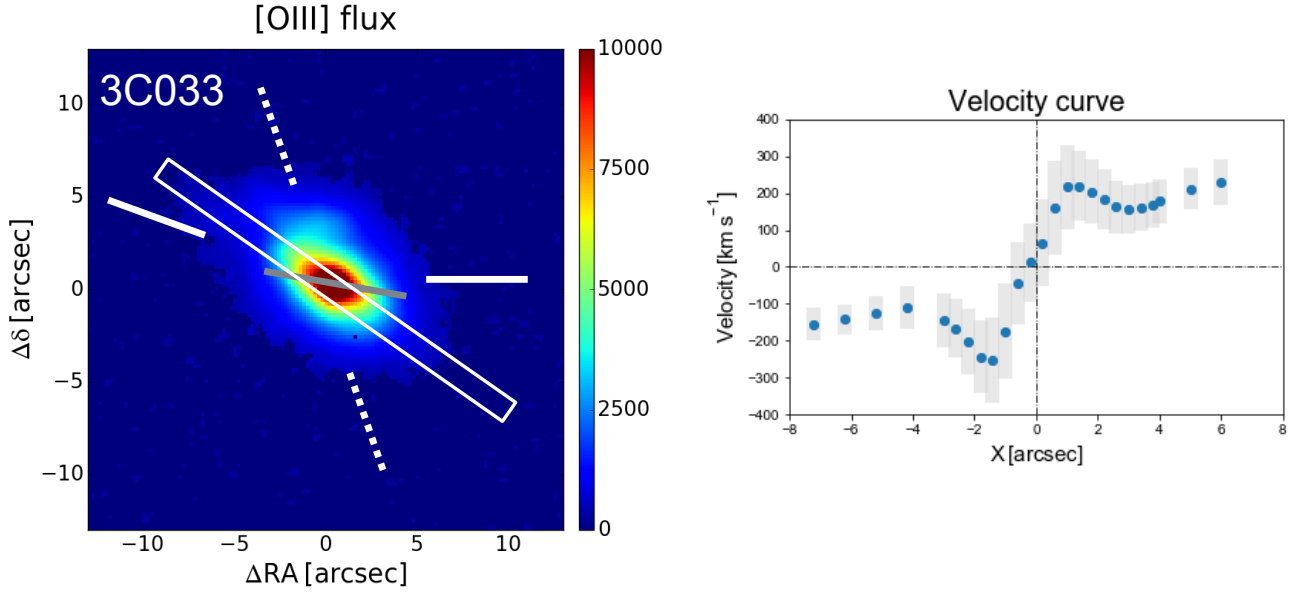


Fig. 1. Example of the emission line properties. *Left:* [O III] emission line image of 3C 33. The white dotted lines mark the radio position angle, the solid white lines show the orientation of the emission line structures on both sides of the nucleus, and the gray line marks the orientation of the kinematical axis in the inner regions measured with kinemetry (see Sect. 2.2). The rectangle represents the region from which we extracted the velocity curve shown in the *right panel*. Data were extracted on each $0''.2$ pixel in the innermost regions and then at distances of $1''$. The length of the gray bars represents the line width at each location.

2.1. Emission lines' orientation and size

In order to estimate the extent and the orientation of the ionized gas structures, we produced a polar diagram for each source, centered on the continuum peak. In Fig. 2 we present the case of the [O III] emission line in 3C 33 as an example. The contour levels are drawn starting from three times the root mean square of the images. In each source we measured the distance and position angle of the faintest emission line structure on both sides of the nucleus. The PA and radius measurements are given in Table 1. The uncertainties are typically of $\sim 10^\circ$. The polar diagrams for all sources are presented in Appendix B.

In the sample there are ten FR I sources: all the FR Is for which it is possible to derive a spectroscopic classification are LEGs. In five of them, the line emission is unresolved or barely resolved and it extends only to a radius of ≤ 1 kpc, while in four sources the EELR reaches distances between 0.5 and 8.8 kpc. The only FR I with an EELR extending beyond the size of the host galaxy is 3C 348 (also known as Hercules A), which shows an elongated morphology reaching a radius of ~ 28 kpc. A detailed morphological study reveals that this source has a hybrid FR I/FR II (e.g., Gizani et al. 2005). All but one (3C 318.1, see Giacintucci et al. 2007; Jimenez-Gallardo et al. 2021 for detailed studies of this source) of the remaining 27 objects are FR II radio galaxies.

The spectroscopic diagnostic diagrams are commonly used to address the gas ionization mechanism by comparing the strength of various emission lines (e.g., Heckman 1980; Baldwin et al. 1981; Veilleux & Osterbrock 1987; Kewley et al. 2006; Law et al. 2021) and to classify AGNs into different classes. Here, we adopt the spectral classification derived for the sources of the sample derived by Buttiglione et al. (2010, 2011). From the point of view of their optical spectroscopic properties, six of them are classified as broad line objects (BLOs), 12 are HEGs, six are LEGs, one (3C 198) has optical diagnostic line ratios typical of star-forming galaxies, while the emission lines in 3C 386 are too weak for such a classification.

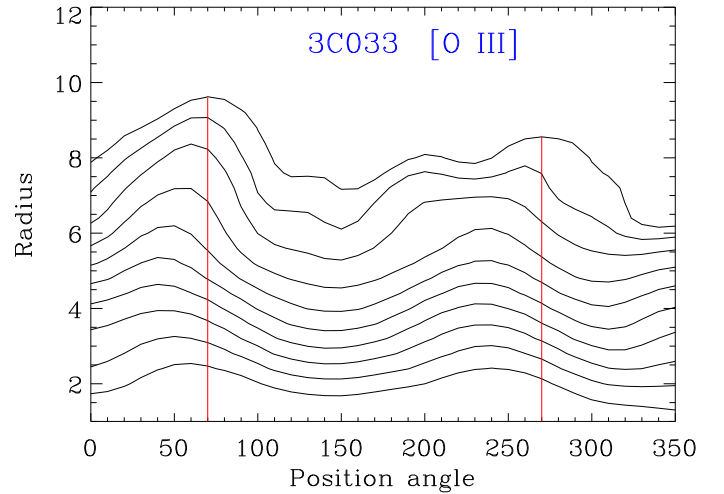


Fig. 2. Polar diagram of the [O III] emission line in 3C 33. Contour levels are drawn starting from three times the root mean square of the images and increase in geometric progression with a common ratio of two. The red solid lines mark the ionized gas position angle on each side of the nucleus.

All the FR II show extended line emission, with the only exceptions being 3C 105 and 3C 456. The sizes of the EELRs range from ~ 4 to ~ 80 kpc, with a median of ~ 16 kpc. As we already discussed in Balmaverde et al. (2021), there are no apparent connections between the EELRs' sizes and luminosities with the spectral classification.

2.2. Central gas kinematics

We fit the 2D gas velocity field in the innermost regions with the kinemetry software (Krajinović et al. 2006), a generalization of surface photometry ellipse fitting which reproduces the moments of the line-of-sight velocity distributions. The

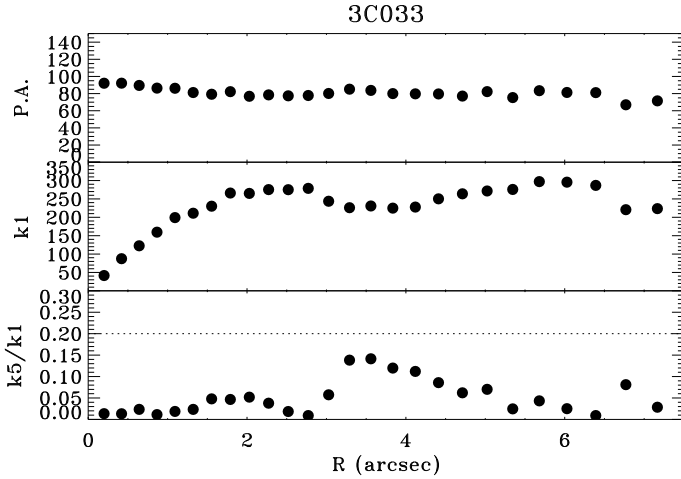


Fig. 3. Results obtained for 3C33 with the kinemetry software (Krajnović et al. 2006). From top to bottom: kinematical position angle PA (in degrees), the $k1$ parameter, corresponding to the amplitude of the rotation curve (in km s^{-1}), and the ratio between the fifth and first coefficient $k5/k1$, which quantifies the deviations from ordered rotation.

parameters of interest returned by this software are as follows: (1) the kinematical PA; (2) the coefficient of the harmonic expansion $k1$ from which one derives the rotation curve; and (3) the ratio between the fifth and first coefficient $k5/k1$, which quantifies the deviations from purely ordered rotation and which is sensitive to the existence of multiple kinematic components. As an example, in Fig. 3 we show the results obtained for 3C33, while the diagrams for all other sources are in Appendix C.

We considered as reliable only the measurements of the kinematical parameters in the sources where these are defined, at least in one point, at a radius $r > 2''$ (i.e., three times the typical seeing of the observations) and where $(k5/k1 + \sigma_{k5/k1}) < 0.2$. According to this, we detected central rotating gas in five out of ten FR Is and in 20 out of 26 FR IIs. We measured the kinematical PA as the median of the values fulfilling the above criteria, a region that extends in most cases to $3''$ – $5''$. The angles of the kinematical major axis are listed in Table 1. The uncertainties are usually between 5° and 10° .

2.3. Kinematics of the large-scale gas

The kinematics of the large-scale gas is often complex and usually cannot be described by a simple rotation model. To investigate its kinematical properties, we extracted a position-velocity diagram and obtained the velocity curve from a synthetic slit aligned along the most extended line structure. While the gas on smaller scale (up to a few kiloparsecs) is very often in ordered rotation, this behavior is rarely seen on a scale of tens of kiloparsecs. This is the case for 3C33, 3C79, 3C300, 3C327, and 3C403, where the whole EELR (extending for between 10 and 35 kpc) follows a smooth rotation curve. In other sources, the central portion of the emission line region shows ordered rotation, while the velocity field at larger distances is disturbed (e.g., in 3C76.1, 3C272.1, and 3C348). In other galaxies, there is a general symmetry in the velocity field, with one side of the EELR being redshifted and the opposite side blueshifted (e.g., in 3C98, 3C180, and 3C227, 3C386), but with large changes in the velocity on small scales.

2.4. Measurements of the host galaxy major axis

We explore the connection between the radio and host galaxy morphology by analyzing their optical and infrared continuum images. Most of the images used were obtained from the near-infrared HST snapshot survey of the 3C sample (Madrid et al. 2006), taken with the $F160W$ broadband filter and less affected by the presence of dust absorption. For some objects, these are not available and we thus used the images taken with WFC2/HST with the broad red filter $F702W$ instead. We fit elliptical isophotes to each image and derived the PA of the host’s major axis reported in Table 1. The uncertainties were derived from the PA variations at different radii and are usually between 5° and 10° .

In two objects (3C445 and 3C456), the optical emission is dominated by their bright nuclei, while in the case of 3C459 the host morphology is highly disturbed. For these galaxies no meaningful estimate of the stellar PA is possible.

3. The geometric connection between radio and line emission

We analyze the geometric connection between the ionized gas with the radio emission, also considering the information derived from the 2D velocity field measured on different scales and the information derived on the host major axis. In the left panel of Fig. 4, we show the offset between the radio axis and the gas position angle as well as the kinematical axis estimated with kinemetry listed in Table 1. When measurements are possible for a given source on both sides of the nucleus, the two offsets values are connected with a vertical line.

The right panel reproduces the various offsets’ distributions. The Kolmogorov–Smirnov test indicates that, by adopting a 5% threshold, none of them are significantly different from a uniform distribution². Nonetheless, the offset between the radio and EELRs’ axis is larger than 45° in 18 out of the 29 sources for which we are able to obtain this measurement. The probability of having this fraction, or a higher fraction, of misaligned sources, estimated via the binomial distribution is $P = 0.13$. There are instead 14 galaxies in which the offset between the radio and kinematic axis is $>45^\circ$ and ten where this is $<45^\circ$ (corresponding to $P = 0.27$). By only considering the FR II sources (13 against six), we obtained a probability of $P = 0.08$. Conversely, there is an equal number of galaxies in which the difference between the PA of the EELRs and of the host galaxy is larger or smaller than 45° .

In summary, we find a weak preference for the EELRs to be oriented at a large angle from the radio axis. An effect is also found for the rotation axis of the innermost gas structures in the FR IIs, while no connection is found with the host axis.

4. The 2D connection between radio and line emission

The statistical analysis presented in the previous sections does not completely grasp the full complexity of the connection between the host galaxy, the radio ejecta, and the properties

² The Kolmogorov–Smirnov test returns a probability of $P = 0.20$ when comparing the radio–EELR offsets with a random distribution, a value that decreases to $P = 0.16$ for the FR IIs. The test applied to the kinematical axis gives $P = 0.37$ for the whole sample and $P = 0.14$ for the FR IIs and $P = 0.98$ for the offset with the host major axis ($P = 0.79$ for the FR IIs).

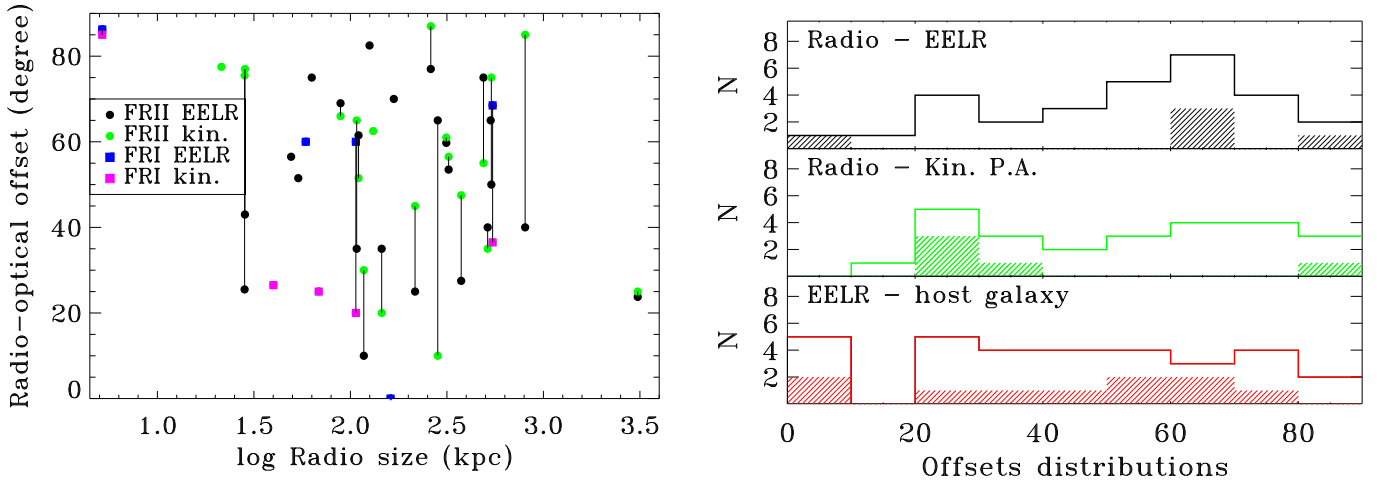


Fig. 4. Comparison of the radio and optical axis. *Left:* offsets between the position angle of the most extended line structure and the radio axis against the LAS of the radio sources. FR Is are marked with blue squares. The green circles are the offsets between the radio and the kinematical axis derived from kinemetry for the FR IIs (magenta squares are for the FR Is). The vertical lines connect the two offsets measurements for the same source when both are available. *Right:* distributions of the offsets of the radio axis from (*top*) the emission line structures, averaged between the two sides, (*center*) the kinematical axis, and (*bottom*) the host's major axis. The shaded area of the histograms is the contribution of the FR Is.

of the ionized gas. In order to explore these issues in more detail, we superposed radio maps onto the 2D velocity maps obtained from the MUSE data. In Fig. 5 we show a subset of representative sources, ordered to present the various behaviors. The remaining images with extended emission line regions are shown in Appendix D and ordered according to their right ascension.

The first row shows the three sources in which the emission line region is located at the edges of the radio lobes. In this category, we include 3C 63, 3C 196.1, as well as 3C 277.3, a source not included in the MURALES sample (since its declination is larger than the limit of our survey), but for which we obtained MUSE observations (Capetti et al. 2022, but see also Miley et al. 1981; Tadhunter et al. 2000; Solórzano-Iñarrea & Tadhunter 2003 for previous emission line images of this source). A similar behavior is also seen in 3C 317 (Balmaverde et al. 2018). Both the morphology and the kinematics of the emission-line gas strongly suggest that in these sources we are seeing the effects of the expanding radio lobes: the radio ejecta compress the external gas, increasing its emissivity and forming shells of line emission with a bubble-like morphology surrounding the radio structure. They are all FR II sources, with a LAS of $\sim 50\text{--}60$ kpc, which is three times smaller than the median size of the FR IIs in the sample.

In the second row, we show three FR I sources. In the first two objects (3C 76.1 and 3C 272.1), we detect a small-scale structure ($\lesssim 4$ kpc in size) of ionized gas perpendicular to the radio jets, showing an ordered rotation with a kinematic axis aligned with the jets. The emission line images of two further FR Is (3C 78 and 3C 264) are barely resolved, but similarly show an ordered velocity field at the center, with an axis displaced by $\sim 25^\circ$ from the radio axis. In 3C 348, the gas is also in ordered rotation, but it is oriented along the jets.

A very similar behavior is seen in the three FR II sources shown in the third row, with quasi-linear structures, close to perpendicular to the radio jets. While the velocity field in 3C 18 is very complex, the remaining sources show a general symmetry. An analogous morphology is seen in 3C 327 that is also characterized by a symmetric rotation curve. The main difference with respect to the FR Is presented above is the larger size of these features, with radii between 15 and 40 kpc.

Similar structures are also seen in the three FR IIs presented in the fourth row. In these cases, however, additional emission line structures are also present. They are mostly located at the edges of the inner portion of the radio lobes. For example, in the case of 3C 79, the emission line region is dominated by a large-scale (~ 70 kpc in size) rotating gaseous structure, but there is also a filament of ionized gas wrapping around the northern edge of the eastern radio lobe, reaching a distance of ~ 80 kpc. The effect of the lateral expansion of the radio lobes far from the radio jet axis has been observed in other radio galaxies (e.g., in 3C 171 and 3C 265, Solórzano-Iñarrea & Tadhunter 2003). A somewhat similar structure is also seen in 3C 227 and 3C 424. In these cases, the emission line region surrounding the radio lobe is the most extended structure: the measurements of the EELR position angle derived in the previous section refer to these components that are aligned within $25^\circ\text{--}40^\circ$ to the radio axis. These sources can be interpreted as a morphological combination of the objects presenting shells surrounding the radio lobes and those dominated by an ionized gas perpendicular to the radio jets.

Finally, in the fifth row, we show three sources (3C 98, 3C 300, and 3C 403) in which the brightest structures of ionized gas are oriented at a small angle ($\Delta PA \lesssim 40^\circ$) from the radio jets. A similar morphology is seen in 3C 33 and 3C 180. Three of them have a clumpy morphology and the velocity field is complex, while 3C 33 and 3C 403 have a smooth disk-like morphology and show well-ordered rotation (for 3C 33, see also Couto et al. 2017). Interestingly, 3C 403 is an X-shaped radio source and the emission line is perpendicular to the secondary radio wings. A statistical tendency for the very extended emission-line gas to align with the radio axis has been observed preferentially in small radio sources (Baum & Heckman 1989b).

5. Ionization properties of the extended emission line regions

Thanks to integral field spectroscopic data, we can explore the gas ionization properties in different portions of the EELRs by comparing the strength of the various emission lines (e.g., Singh et al. 2013). Since this approach requires one to detect several emission lines in each spaxel, we extracted spectra from

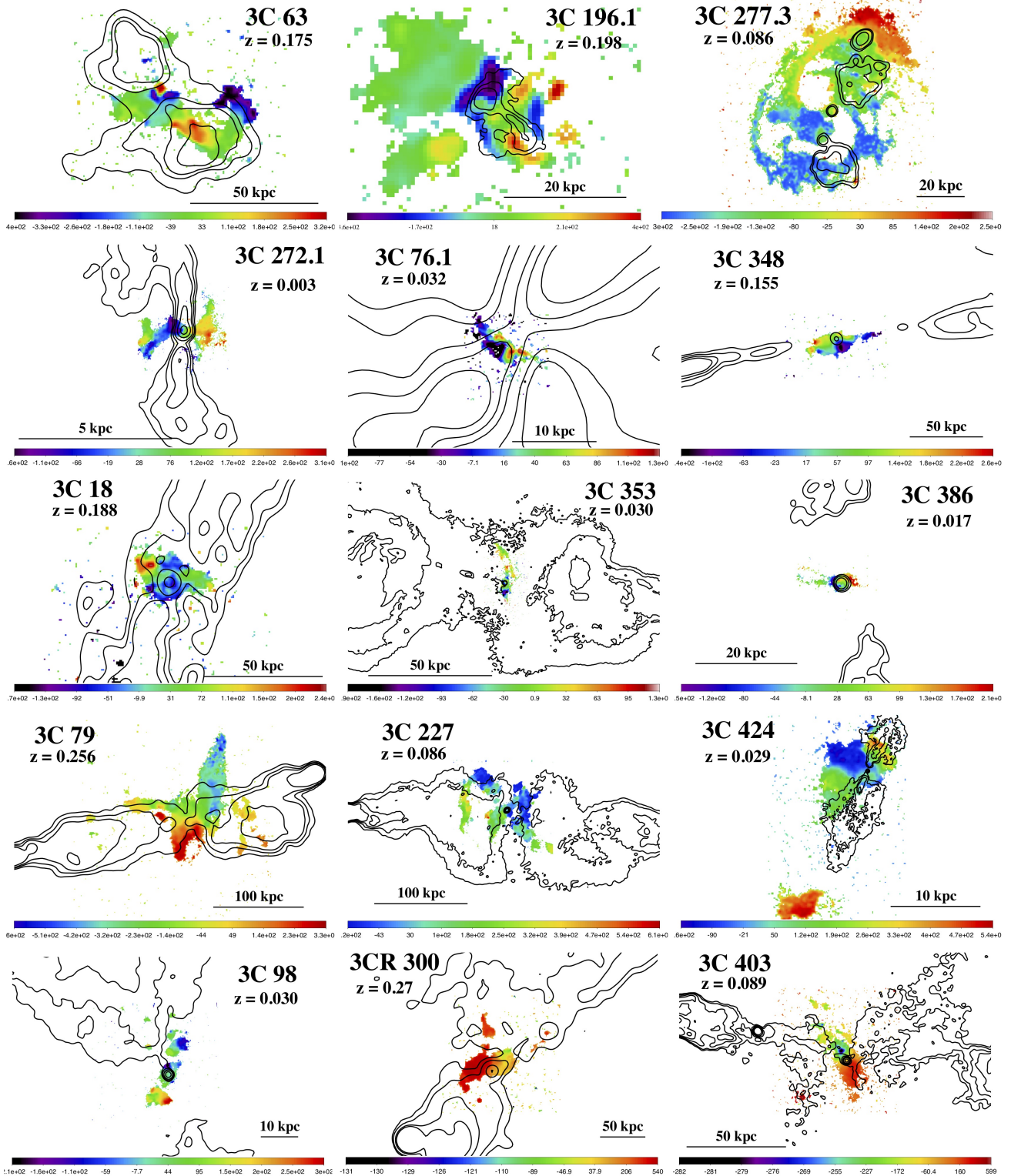


Fig. 5. Superposition of the radio contours onto the ionized gas velocity maps.

synthetic apertures as far as possible from the nuclei, but still in regions with a sufficient signal to derive useful measurements. In [Balmaverde et al. \(2019\)](#), we already presented this analysis for a subsample of 20 3C sources: we discarded the sources in which the emission line region is only marginally extended to obtain off-nuclear measurements and we were left with useful data for 14 sources. By applying the same method to the new

list of 17 objects, we can study the ionization properties of the off-nuclear gas in eight further sources. In 3C 079 and 3C 227, the EELR extends in both the parallel and perpendicular direction from the radio axis and we then extracted spectra in two off-nuclear regions. The spectra of these regions are shown in [Appendix E](#). The selected areas, which are located at a median distance of ~ 15 kpc from the nucleus, but reaching distances of

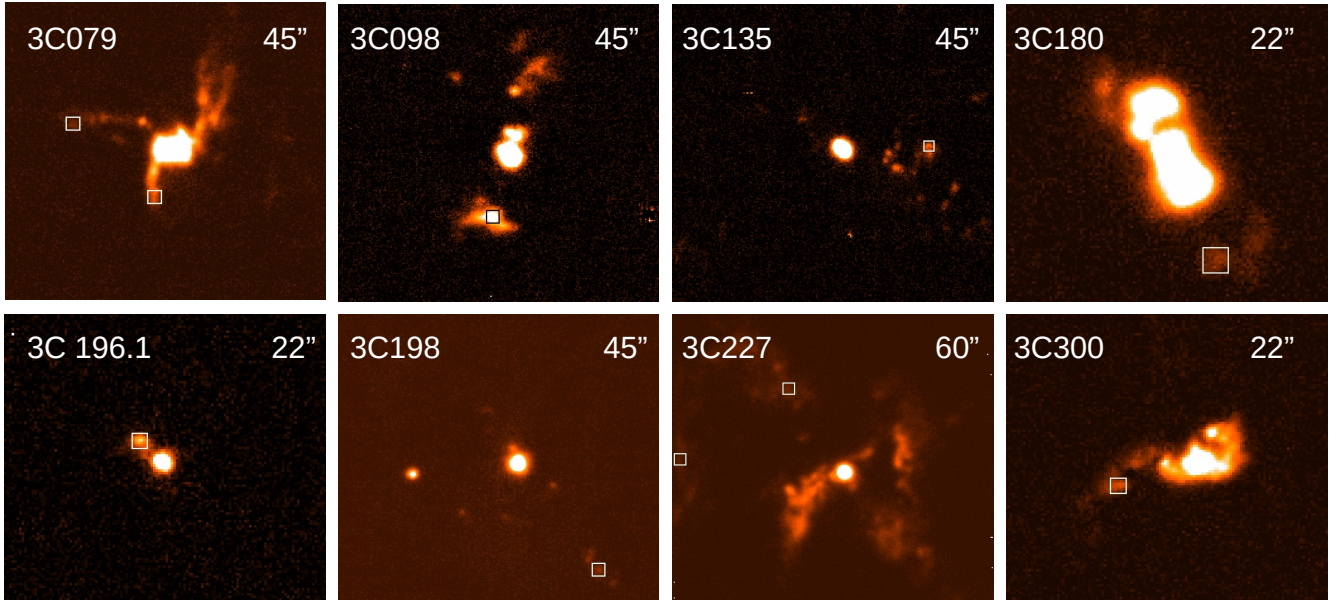


Fig. 6. Emission line images (in logarithmic scale) of the eight radio galaxies observed presented by [Balmaverde et al. \(2021\)](#) in which we were able to extract off nuclear spectra. Images of the remaining 14 sources are shown in [Balmaverde et al. \(2019\)](#). The fields of view are indicated in the upper left corner of each image. The white boxes mark the synthetic aperture from which we extracted the spectra.

~ 80 kpc, are marked in Fig. 6. In Table 2 we list the line ratios for each region and derive a spectroscopic classification based on the location in the diagnostic diagrams defined by [Kewley et al. \(2006; Fig. 7\)](#).

Most of the sources (15 out of 22, all of them FR II) considered are HEGs; this also includes the BLOs whose narrow emission line ratios are characteristic of high excitation gas in this class. In many of them, the off-nuclear region we considered for this analysis is located at a large angle with respect to the radio axis. In 3C 327, for example, it is almost perpendicular to the radio axis, while in four other sources the offset is $\sim 60^\circ$. In 13 of them, the large-scale gas also has a HEG spectrum. Similarly, in three of the four LEGs, the extended gas has a low excitation spectrum; also, in the only star-forming RG of the sample (3C 198), the large-scale emission has line ratios consistent with photoionization by young stars.

However, there is one HEG, 3C 458, in which the emission line ratios measured on the extended emission correspond to a different spectroscopic type, for which we derived a LEG classification. In this case, the extended emission line region is located at a very large distance from the nucleus (80 kpc). The transition from high to low ionization appears to occur gradually based on the decrease of the $[\text{O III}]/\text{H}\alpha$ ratio with distance.

Finally, there are four sources with a peculiar behavior, namely 3C 63 (a HEG), 3C 318.1 and 3C 386 (both of uncertain spectral type), and 3C 424 (a LEG): they are located in different regions of the diagnostic diagrams depending on the panel considered, an indication that we might be observing regions in which photoionization from an active nucleus or from young stars is not the dominant process. This is reminiscent of the results found with MUSE observations by [Balmaverde et al. \(2018\)](#) for 3C 317: we argued that ionization in that source is due to slow shocks ([Dopita & Sutherland 1995](#)) or collisional heating from cosmic rays ([Ferland et al. 2008, 2009; Fabian et al. 2011](#)). The general small velocity dispersion of the emission lines in these regions, $\sim 50\text{--}100$ km s $^{-1}$, argues against the importance of shocks, thus favoring ionization from energetic particles.

In the two RGs in which the EELRs have an X-shaped morphology (namely, 3C 079 and 3C 227), we were able to extract off-nuclear spectra along different angles, almost parallel and perpendicular to the radio jet, respectively. In both cases, the emission line ratios in the two regions are extremely similar. In particular, in 3C 227, the spectrum of the region located at a projected angle of 9° from the radio axis share essentially the same location in the diagnostic diagrams of the region 62° away from it.

6. Discussion

The kinematics and the distribution of ionized gas and its connection with the radio emission provides us with a powerful tool to explore its origin and the effects of the active nucleus onto the external medium, that is, the process of feedback in radio-loud AGNs.

6.1. Gas geometry and kinematics

From the point of view of gas geometry, we confirm the previous results that, in low redshift RGs, the radio and line alignment is rather weak, contrarily to what is observed in more distant and luminous sources. More specifically, we find a preference of the more distant emission line structure to be located at an angle larger than 45° relative to the radio axis; this occurs in 18 out of the 29 sources in which we were able to perform this comparison. In most cases of these “misaligned” sources, the EELR takes the form of a disk-like (elongated or filamentary) structure, usually extending for several tens of kiloparsecs. In some of the “aligned” objects, bubbles of gas enshroud the radio lobes, clearly indicative of a direct impact of the jets on the external medium; in these galaxies, the radio source is three times smaller ($\sim 50\text{--}60$ kpc) than the average size of the sample, suggesting that this process occurs in the early phase of their evolution. The smaller size of these sources can also be caused by the denser environment in which the jets propagate. In addition, there is a group of sources in which, similarly, filamentary

Table 2. Synthetic aperture for the off-nuclear spectra and diagnostic line ratios.

| Name (type) | Size | Distance (") | | (kpc) | Offset | [O III]/H β | [N II]/H α | [S II]/H α | [O I]/H α | Type |
|-----------------------|------|--------------|--------|-------|--------|-------------------|-------------------|-------------------|------------------|----------|
| 3C 017 (BLO) | 1.2 | 2.4 W | 0.0 N | 10.5 | 66 | 4.74 | 0.74 | 0.64 | 0.31 | HEG |
| 3C 018 (BLO) | 2.0 | 3.4 W | 0.6 N | 13.0 | 63 | 16.72 | 1.11 | 0.60 | 0.13 | HEG |
| 3C 033 (HEG) | 2.0 | 4.0 E | 3.6 N | 6.3 | 29 | 14.54 | 0.34 | 0.26 | 0.12 | HEG |
| 3C 063 (HEG) | 4.0 | 8.6 W | 1.4 S | 30.1 | 48 | 1.18 | 0.30 | 0.52 | 0.22 | Peculiar |
| 3C 079 (HEG) A | 2.0 | 2.6 E | 7.4 S | 56.6 | 56 | 12.43 | 0.38 | 0.25 | | HEG |
| J | 2.0 | 10.0 E | 1.0 N | 56.0 | 21 | 6.63 | 0.59 | 0.41 | 0.30 | HEG |
| 3C 098 (HEG) | 2.0 | 2.8 E | 9.6 S | 6.0 | 41 | 11.90 | 0.18 | 0.17 | | HEG |
| 3C 135 (HEG) | 1.6 | 14.0 W | 0.0 S | 31.6 | 15 | 13.54 | 0.88 | 0.59 | 0.16 | HEG |
| 3C 180 (HEG) | 2.0 | 8.8 W | 14.2 S | 59.8 | 22 | 8.22 | 0.48 | 0.49 | 0.10 | HEG |
| 3C 196.1 (LEG) | 1.2 | 2.0 E | 2.0 N | 9.3 | 0 | 2.33 | 1.23 | 1.00 | 0.42 | LEG |
| 3C 198 (SF) | 1.2 | 12.6 W | 17.0 S | 32.6 | 7 | 1.46 | 0.25 | 0.37 | 0.09 | SF |
| 3C 227 (BLO) J | 2.0 | 28.4 W | 2.2 N | 46.1 | 9 | 6.94 | 0.40 | 0.43 | 0.12 | HEG |
| A | 2.0 | 9.6 W | 14.8 N | 28.6 | 62 | 7.30 | 0.47 | 0.32 | 0.08 | HEG |
| 3C 300 (HEG) | 2.0 | 3.6 E | 2.0 S | 17.2 | 13 | 9.90 | 0.23 | 0.30 | 0.10 | HEG |
| 3C 318.1 (-) | 1.6 | 0.4 E | 13.0 S | 11.7 | - | 0.23 | 1.24 | 0.43 | 0.16 | Peculiar |
| 3C 327 (HEG) | 2.0 | 0.4 E | 3.8 N | 8.1 | 86 | 11.64 | 1.33 | 0.75 | | HEG |
| 3C 353 (LEG) | 4.0 | 0.8 E | 19.8 N | 12.7 | 80 | <1.90 | 0.66 | 0.69 | | LEG |
| 3C 386 (-) | 4.0 | 11.4 E | 0.0 N | 4.2 | 74 | 0.66 | 1.01 | 0.28 | | Peculiar |
| 3C 403 (HEG) | 4.0 | 6.8 E | 6.6 N | 11.3 | 40 | >9.50 | 1.15 | 0.72 | | HEG |
| 3C 424 (LEG) | 4.0 | 5.8 E | 6.8 S | 2.4 | 15 | 0.77 | 0.68 | 0.58 | 0.18 | Peculiar |
| 3C 442 (LEG) | 1.2 | 0.4 W | 4.6 S | 3.0 | 58 | >0.52 | 3.00 | 1.74 | 0.40 | LEG |
| 3C 445 (BLO) | 4.0 | 11.8 W | 9.8 S | 17.0 | 57 | 8.20 | 0.15 | 0.35 | 0.08 | HEG |
| 3C 458 (HEG) | 2.0 | 7.8 E | 11.6 N | 80.2 | 41 | 5.60 | 0.58 | 0.99 | 0.53 | LEG |
| 3C 459 (BLO) | 1.2 | 12.4 W | 9.8 N | 69.0 | 31 | 5.50 | 0.18 | 0.68 | | HEG |

Notes. Column description: (1) source name (we report the sources for which we obtained new measurements in boldface) and spectroscopic classification. For 3C 079 and 3C 227 we considered two regions, across (A) and along (J) the jet; (2) region size (arcseconds); (3) distance of the region considered from the nucleus in arcseconds and (4) kpc, (5) angular offset between the radio axis and the fitted region (6), (7), (8), and (9) diagnostic line ratios, (10) spectroscopic classification of the extended region.

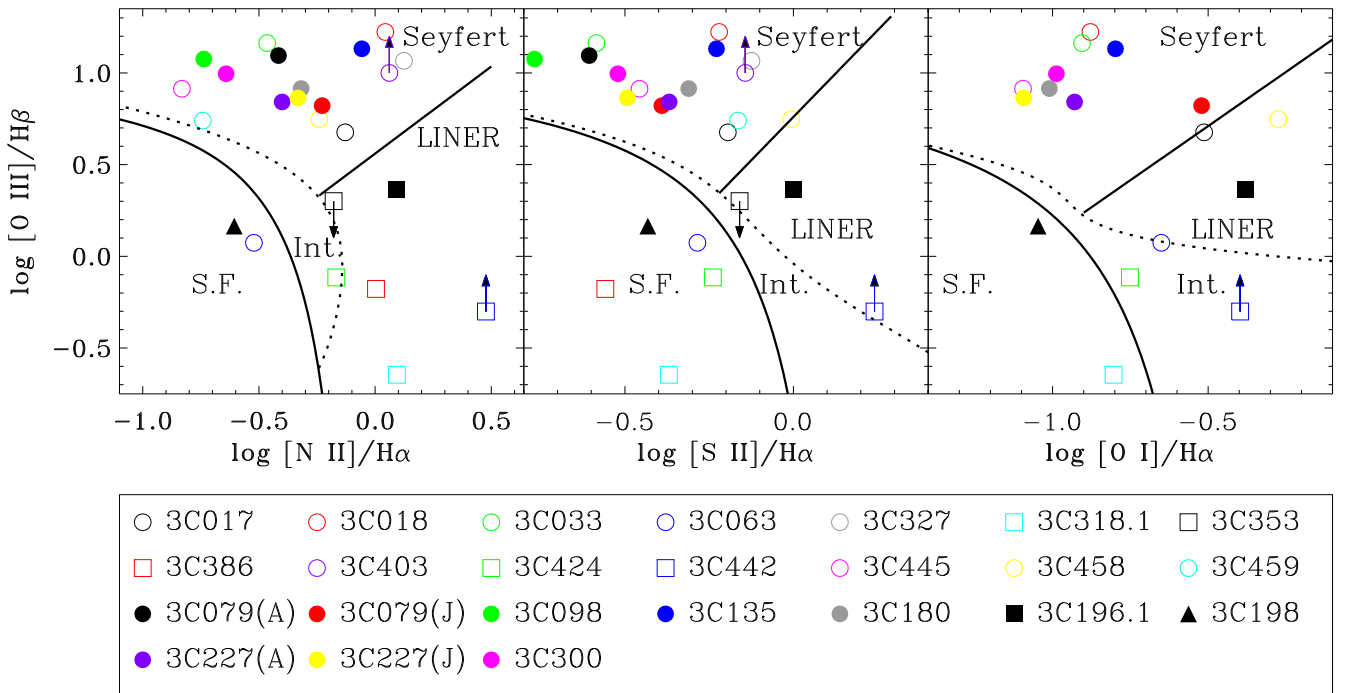


Fig. 7. Location of the 22 FR II radio galaxies with extended line emission in the spectroscopic diagnostic diagrams. Circles (squares) correspond to sources classified as HEGs (LEGs or unclassified) based on their nuclear emission line ratios (Buttiglione et al. 2010). The solid curves separate star-forming (S.F.) from intermediate galaxies (Int.), the dotted curve separates intermediate galaxies from AGNs. The black lines separate low and high excitation galaxies, LEGs and HEGs, respectively (Law et al. 2021).

structures follow the edges of the radio source leading to a general alignment, but disk-like structures are present on a smaller scale. These structures can be interpreted as “remnant” bubbles, produced in earlier phases of the source expansion, and left behind now that the radio jets reached sizes of several hundreds of kiloparsecs.

From the point of view of gas kinematics, the analysis performed with the kinemetry code revealed gas in ordered rotation, suggestive of the presence of a disk of a few kiloparsecs, in 77% of the FR IIs (20 out of 26) and in 50% of the FR Is (five out of ten, but in several FR Is the emission is unresolved and no kinematic study is possible). The misalignment between the radio and rotation axis is stronger than was found for the morphology, in particular for the FR IIs where 13/19 sources show an offset larger than $\sim 45^\circ$. This, again, is in line with previous results (Baum & Heckman 1989b; Solórzano-Iñiarrea & Tadhunter 2003).

6.2. The gas ionization mechanism

A significant point is the identification of the ionization mechanism of the warm extended gas. We measured the off-nuclear emission (with a median distance of 15 kpc) line ratios in 22 sources of the sample where the line emission is sufficiently well resolved. In most cases (15), these are HEGs from the point of view of their nuclear properties and we also found emission line ratios typical of HEGs in the EELR of 13 sources. This suggests that on both scales, we are observing gas photoionized by the central source. However, the angle that formed by the radio axis (most likely, coincident with the axis of the nuclear ionizing radiation field) and that leading to the off-nuclear region is large, between 30° and 85° , with a median of 60° . Along these lines of sight, the nuclear ionizing radiation should be blocked by the circumnuclear torus (Antonucci 1993). The presence of this absorbing material is confirmed by the X-ray nuclear spectra of several of these sources showing large columns of cold gas (Massaro et al. 2012, 2015). The study of Baldi et al. (2013), based on the relative number of 3C sources with $z < 0.3$ with and without broad lines in their optical spectra, indicates a covering factor of the circumnuclear matter of 65% that corresponds, adopting a torus geometry, to an opening angle of $50 \pm 5^\circ$. The regions outside this bicone should not be illuminated by the nuclear radiation field, contrary to what is observed. However, projection effects might play a significant role, particularly considering that the ionized gas is most likely only a small component of a much more massive gaseous structure. It is also possible that we are witnessing the effects of the expanding radio lobes that are compressing and ionizing the intergalactic medium: sufficiently fast shocks (with velocities of several hundreds of km s^{-1}) produce line ratios compatible with those seen in the EELR of the RGs (Allen et al. 2008). However, at these large angles from the path of the radio jets, such high velocities are unlikely to be reached. Overall, we must therefore conclude that the ionization mechanism of the EELR remains unclear in general.

6.3. Evidence for superdisks in radio galaxies

A novel result of our analysis is the widespread presence, with only a few exceptions, of large structures of ionized gas with sizes up to ~ 80 kpc, usually with a highly elongated and filamentary morphology. Gopal-Krishna & Wiita (2000) argued that various pieces of evidence point to the presence of a large gaseous disk associated with radio-loud AGNs: the dust absorption fea-

tures seen in several nearby RGs, the sharp edges of the radio lobes on the side facing the host, the asymmetry of Ly α nebulae in high redshift radio galaxies. Given the estimated sizes of such structures ($\sim 75 \text{ kpc} \times 25 \text{ kpc}$), they defined them as superdisks. They suggested that these structures are tidally stretched remnants of gas-rich mergers. Large disks of neutral hydrogen are commonly seen in early-type galaxies, often stretching to many tens of kiloparsecs (Serra et al. 2012). The results of the MUSE observations provide direct evidence that such superdisks are indeed present in the majority of the nearby RGs. Both the morphology (with filamentary and irregular structures) and the kinematics (in about half of the sources the gas kinematics is complex, with large velocity changes on small scales) of the ionized gas indicates that the gas is not in a relaxed state. This is probably due, in part, to the long timescale for the gravitational settling of these large-scale structures, but also to the impact of the radio emitting outflows.

6.4. Jets and gas interactions and evolution of radio galaxies

Overall, the different properties of the EELR can be explained with a combination of the source evolutionary state and the orientation of the superdisk with respect to the radio axis (see Fig. 8 for a schematic view). As long as the radio source is smaller than the vertical height of the superdisk, it propagates into a dense environment and it forms bubbles of gas, visible as expanding shells in the emission line images (for example in 3C 63, 3C 196.1, 3C 277.3, and 3C 317). This situation is reminiscent of the process at the origin of the radio and line alignment commonly observed on smaller scales in the young, compact steep spectrum sources (CSS, de Vries et al. 1997, 1999; Axon et al. 2000). In some cases, the bubbles that formed in the initial stages are still visible in larger radio sources as filaments surrounding the lobes (e.g., in 3C 79). The subsequent evolution depends on the orientation of the radio jets with respect to the superdisk axis. At high inclination, when the jets have escaped from the denser regions, the EELR is dominated by a disk structure; at least on a scale of a few kiloparsecs, it shows ordered rotation at a large angle from the radio axis. In sources where the jets propagate at a small angle with respect to the plane of the disk, strong jet-cloud interactions occur and the EELR has an arc-like or clumpy morphology. This is clearly seen in 3C 180 in both the MUSE and the HST emission line images (Baldi et al. 2019). A clumpy EELR, such as observed in 3C 98 and 3C 300, might result when the jet grazes the superdisk.

The radio and optical alignment observed in high redshift RGs can also be understood in this scenario. High- z RGs are known to be smaller than those at low z (e.g., Saxena et al. 2017 and references therein) and they propagate in a denser environment. The putative superdisks associated with these sources are also likely to be farther from a settled state. The reduced sizes of high- z RGs and the different properties of the external medium favor the possibility of enhanced jet-cloud interactions and might lead to a higher fraction of radio and optical aligned sources.

The interaction between the relativistic outflow and an external gas disk presented above is in line with the results obtained from the numerical simulations performed by Mukherjee et al. (2018) in which a relativistic jet interacts with a dense turbulent gaseous disk. The main difference between the data and the simulations relies on the scale heights of the superdisks, which are an order of magnitude larger than those adopted in their model. This implies a correspondingly longer timescale (~ 1 Myr for the simulations) over which the jet-cloud interactions are effective. Nonetheless, the temporal evolution and the relevance of the

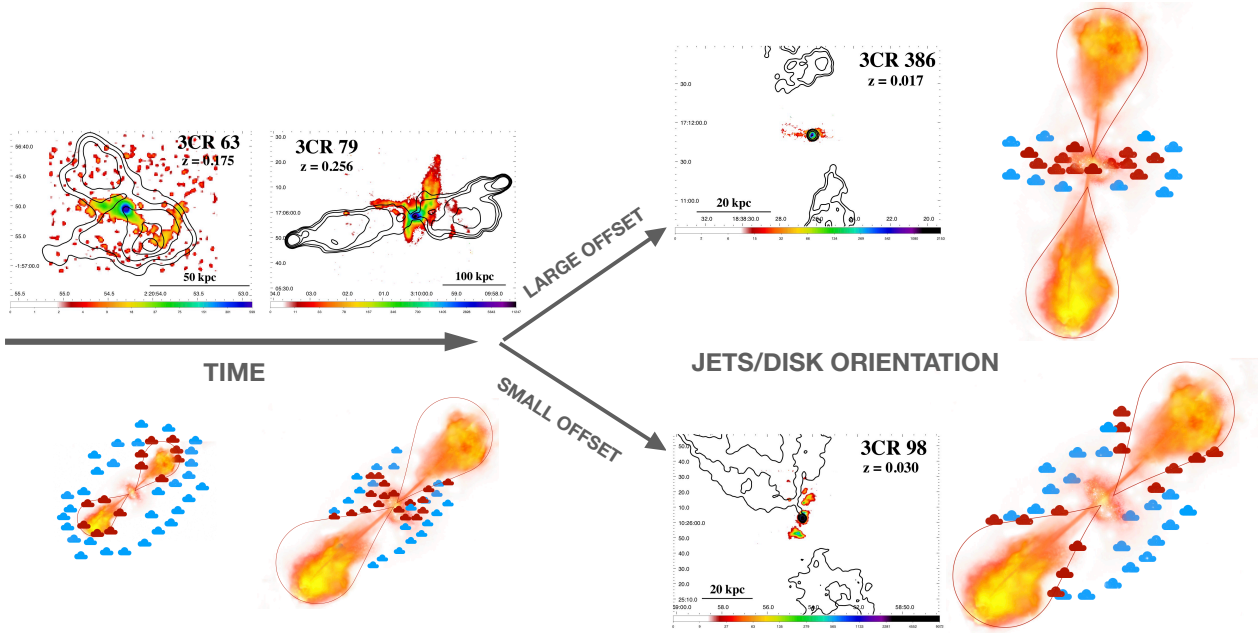


Fig. 8. Schematic view of the evolution of the ionized gas structure. In the initial stages, the expanding radio lobes form a bubble of ionized gas (red clouds). When the radio source has escaped the superdisk, the remnants of the bubble are still visible as filaments around the base of the lobes, but the main structure is a rotating disk. The final state depends on the orientation of the superdisk with respect to the radio axis: when they are perpendicular to each other, a linear rotating structure is present; whereas, when the jets form a small angle with the superdisk, clumpy line emission with a complex velocity field is seen, indicative of ongoing strong jet-cloud interactions.

relative jet-gas inclination they derived is fully consistent with our conclusions. It is unclear whether this picture also applies to FR Is. Gaseous and dusty disks are seen in these sources (e.g., Sparks et al. 2000), but with relatively small sizes with respect to FR IIs. This difference can be due to the paucity of gas in FR Is, and also to the lack of photons required to ionize large-scale structures.

Considering the orientation of the ionized gas with respect to the radio axis, we found a preference for the most extended gas to be at an offset larger than 45° , a situation occurring in about two-thirds of the sources analyzed. This fraction actually underestimates the number of sources in which there are linear gas structures at large angles from the jets due to the presence of objects such as 3C 227 and 3C 424 in which we see an elongated gas feature, perpendicular to the radio axis, but this is not the most extended line structure. In addition, in the sources characterized by a shell-like EELR, the observed alignment of the EELR with the radio axis is caused by the jet-cloud interactions and not by the intrinsic gas distribution.

The large angle generally formed between the axis of the radio and the EELR might be produced (or enhanced) by the pressure exerted on the superdisks by the jet material back-flowing from the hot spots toward the nucleus. However, the geometrical link between the structure of ionized gas and the radio jets can also be the result of an intrinsic alignment between the axis of the AGN and the gaseous disk (Bardeen & Petterson 1975; Rees 1978; Scheuer & Feiler 1996; Natarajan & Pringle 1998). This is what is expected when a preferred plane of accretion, defined by the orbital plane of a merging galaxy, is maintained over a large time interval. In this situation, the SMBH is fueled by material with a coherent and stable angular momentum (also including any secondary SMBH) and this tends to align its rotation axis with that of the accreting matter. The resulting geometry of the system also depends on the SMBH spin before the merger: slowly rotating black holes are more easily

reoriented, while SMBH of a higher spin maintain their axis. We speculate that the latter ones are associated with the RGs in which we observed the smaller offset between the radio and gas axis.

6.5. AGN feedback in radio galaxies

A general picture of the interaction between the dense ionized gas and the radio jets emerges from the analysis of the emission line images of the nearby RGs of the 3CR sample. In the early phases of the sources' lifetime, the relativistic jets transfer energy and momentum from the AGN to the external medium that is compressed, accelerated, and displaced. As shown by Speranza et al. (2021), both nuclear and kiloparsec scale outflows of ionized gas are commonly detected in these sources, but they have a limited impact on the gas content or the star formation in the host. Based on the observed emission line ratios, typical of AGN ionization over the whole emission line nebula (with the exception of 3C 277.3 presented in Capetti et al. 2022 and 3C 135), this interaction does not produce detectable star-forming regions. This phase lasts as long as the source is confined within the central tens of kiloparsecs corresponding to the vertical height of the superdisks. In the later evolution, the radio source escapes from the dense central regions and the jet-gas interactions are strongly reduced. The impact of the radio source on the superdisks' gas is then limited to the compression of the back-flowing material, but, as long as the radio source keeps expanding, it will continue to drive shocks and transfer energy to the external gas.

7. Summary and conclusions

In this sixth paper presenting the MURALES survey, we analyze the results obtained from the MUSE observations of 37 3C radio sources with $z < 0.3$. In the FR Is, the ionized gas is confined

to within ≤ 4 kpc, while elongated or filamentary gas structures are seen in all but two of the 26 FR IIs, extending for 10–30 kpc, and showing a broad distribution of offsets from the radio axis.

The gas on a scale of a few kiloparsecs generally shows ordered rotation around an axis forming a median angle of 65° with the radio axis. The kinematics of the large-scale gas is more complex: in half of the sources, the EELR shows a regular velocity field or a general velocity symmetry; however, in the other galaxies, it is more complex, with large velocity changes on small spatial scales.

The large-scale gas generally shows ionization properties similar to those derived for the nucleus. In many sources, these extended structures are located at a large angle from the radio axis: due to the presence of circumnuclear obscuring material, they should not be illuminated by the nucleus. However, shock ionization is unlikely because this gas is located far from the path of the relativistic jets. The ionization mechanism of the large-scale gas remains unclear.

The radio and the gas emission presents a variety of geometrical connections: shells of gas surrounding the radio lobes; linear or filamentary structures, usually forming a large angle with the radio axis; and arc-like or clumpy EELRs forming a small angle with the radio axis. The observed emission line structures in FR IIs can be interpreted as due to the presence of gaseous superdisks, which are remnants of gas-rich mergers. These superdisks, with sizes of several tens of kiloparsecs, have been previously postulated based on various properties of RGs. The variety of morphologies of the EELRs can be accounted for with a combination of the source age and of the orientation of the superdisk with respect to the radio axis. The bubble-like morphology arises when the radio source is in its early phases and confined within the superdisk. At later stages, the EELR properties depend on the relative orientation of jets and superdisks: the sources with a large radio-line offset escape more rapidly from the regions where the ISM is denser; whereas, in those located at smaller angles, the jet-cloud interactions are active for a longer time.

We speculate that the alignment often observed between the axis of the AGN and the gaseous disk might be due to the accretion of material over a large time interval confined to a preferred plane, that is, the orbital plane of the gas-rich galaxy responsible for the formation of the superdisks. This effect tends to align the SMBH spin with that of the accreting matter.

Concerning the AGN feedback, in these nearby radio-loud AGNs, energy is mainly transferred to the ISM during the early phases of their lifetime when this is compressed and heated, but it does not generally lead to star formation. The outflows of ionized gas, commonly detected in these sources, also have a limited impact on the external medium. Nonetheless, the presence of extended gaseous structures possibly associated with superdisks extends the timescale of the impact of the AGNs onto the ISM phase with respect to the previous scenario in which this was confined to the size of the host galaxy, that is, in the CSS phase. However, the warm line-emitting gas represents only a small component of the ISM. A global view of radio feedback also requires one to include the cold ISM phase in the analysis.

Further analysis is also needed concerning the numerical simulations by considering more extended gas distribution with respect to those that have been included so far. It is also of great interest to assess whether superdisks are only present in the powerful radio-loud AGNs, a result that suggests a strong connection between these sources with gas-rich mergers, or whether these are also found in radio-quiet AGNs. Finally, superdisks should also be present in non-active sources if they are observed

after the merger event, but before the onset of the nuclear activity.

Acknowledgements. We thank the referee for her/his useful comments. GS is supported by the European Union’s Horizon 2020 research and innovation programme under Marie Skłodowska-Curie grant agreement No 860744 (BID4BEST). GS acknowledges the project “Feeding and feedback in active galaxies”, with reference PID2019-106027GB-C42, funded by MICINN-AEI/10.13039/501100011033. AM acknowledges financial support from PRIN-MIUR contract 2017PH3WAT. SB and CO acknowledge support from the Natural Sciences and Engineering Research Council (NSERC) of Canada. Based on observations made with ESO Telescopes at the La Silla Paranal Observatory under programme ID 097.B-0766(A). This research has made use of data obtained from the *Chandra* Data Archive. The National Radio Astronomy Observatory is a facility of the National Science Foundation operated under cooperative agreement by Associated Universities, Inc. BB acknowledge financial contribution from the agreement ASI-INAF I/037/12/0. Some of the data presented here are based on observations made with the NASA/ESA *Hubble* Space Telescope, obtained from the data archive at the Space Telescope Science Institute. STScI is operated by the Association of Universities for Research in Astronomy, Inc. under NASA contract NAS 5-26555.

References

- Allen, M. G., Groves, B. A., Dopita, M. A., Sutherland, R. S., & Kewley, L. J. 2008, *ApJS*, **178**, 20
- Antonucci, R. 1993, *ARA&A*, **31**, 473
- Axon, D. J., Capetti, A., Fanti, R., et al. 2000, *AJ*, **120**, 2284
- Baldi, R. D., Capetti, A., Buttiglione, S., Chiaberge, M., & Celotti, A. 2013, *A&A*, **560**, A81
- Baldi, R. D., Rodríguez Zaurín, J., Chiaberge, M., et al. 2019, *ApJ*, **870**, 53
- Baldwin, J. A., Phillips, M. M., & Terlevich, R. 1981, *PASP*, **93**, 5
- Balmaverde, B., Capetti, A., Marconi, A., & Venturi, G. 2018, *A&A*, **612**, A19
- Balmaverde, B., Capetti, A., Marconi, A., et al. 2019, *A&A*, **632**, A124
- Balmaverde, B., Capetti, A., Marconi, A., et al. 2021, *A&A*, **645**, A12
- Bardeen, J. M., & Petterson, J. A. 1975, *ApJ*, **195**, L65
- Baum, S. A., & Heckman, T. 1989a, *ApJ*, **336**, 681
- Baum, S. A., & Heckman, T. 1989b, *ApJ*, **336**, 702
- Baum, S. A., Heckman, T. M., & van Breugel, W. 1992, *ApJ*, **389**, 208
- Bennett, C. L., Larson, D., Weiland, J. L., & Hinshaw, G. 2014, *ApJ*, **794**, 135
- Best, P. N., Röttgering, H. J. A., & Longair, M. S. 2000, *MNRAS*, **311**, 23
- Birzan, L., Rafferty, D. A., McNamara, B. R., Wise, M. W., & Nulsen, P. E. J. 2004, *ApJ*, **607**, 800
- Buttiglione, S., Capetti, A., Celotti, A., et al. 2010, *A&A*, **509**, A6
- Buttiglione, S., Capetti, A., Celotti, A., et al. 2011, *A&A*, **525**, A28
- Capetti, A., Balmaverde, B., Tadhunter, C., et al. 2022, *A&A*, **657**, A114
- Carniani, S., Marconi, A., Maiolino, R., et al. 2016, *A&A*, **591**, A28
- Chambers, K. C., Miley, G. K., & van Breugel, W. 1987, *Nature*, **329**, 604
- Couto, G. S., Storchi-Bergmann, T., & Schnorr-Müller, A. 2017, *MNRAS*, **469**, 1573
- de Vries, W. H., O’Dea, C. P., Baum, S. A., et al. 1997, *ApJS*, **110**, 191
- de Vries, W. H., O’Dea, C. P., Baum, S. A., & Barthel, P. D. 1999, *ApJ*, **526**, 27
- Dopita, M. A., & Sutherland, R. S. 1995, *ApJ*, **455**, 468
- Fabian, A. C. 2012, *ARA&A*, **50**, 455
- Fabian, A. C., Sanders, J. S., Williams, R. J. R., et al. 2011, *MNRAS*, **417**, 172
- Fanaroff, B. L., & Riley, J. M. 1974, *MNRAS*, **167**, 31P
- Ferland, G. J., Fabian, A. C., Hatch, N. A., et al. 2008, *MNRAS*, **386**, L72
- Ferland, G. J., Fabian, A. C., Hatch, N. A., et al. 2009, *MNRAS*, **392**, 1475
- Giacintucci, S., Venturi, T., Murgia, M., et al. 2007, *A&A*, **476**, 99
- Gizani, N. A. B., Cohen, A., & Kassim, N. E. 2005, *MNRAS*, **358**, 1061
- Gopal-Krishna, & Wiita, P. J. 2000, *ApJ*, **529**, 189
- Heckman, T. M. 1980, *A&A*, **87**, 152
- Inskip, K. J., Best, P. N., Rawlings, S., et al. 2002, *MNRAS*, **337**, 1381
- Inskip, K. J., Best, P. N., Longair, M. S., & Röttgering, H. J. A. 2005, *MNRAS*, **359**, 1393
- Jimenez-Gallardo, A., Massaro, F., Balmaverde, B., et al. 2021, *ApJ*, **912**, L25
- Kewley, L. J., Groves, B., Kauffmann, G., & Heckman, T. 2006, *MNRAS*, **372**, 961
- Krajinović, D., Cappellari, M., de Zeeuw, P. T., & Copin, Y. 2006, *MNRAS*, **366**, 787
- Laing, R. A., Riley, J. M., & Longair, M. S. 1983, *MNRAS*, **204**, 151
- Law, D. R., Ji, X., Belfiore, F., et al. 2021, *ApJ*, **915**, 35
- Madrid, J. P., Chiaberge, M., Floyd, D., et al. 2006, *ApJS*, **164**, 307
- Massaro, F., Tremblay, G. R., Harris, D. E., et al. 2012, *ApJS*, **203**, 31
- Massaro, F., Harris, D. E., Liuzzo, E., et al. 2015, *ApJS*, **220**, 5
- McCarthy, P. J. 1993, *ARA&A*, **31**, 639

B. Balmaverde et al.: The MURALES survey. VI.

- McCarthy, P. J., & van Breugel, W. 1989, *Eur. South. Obs. Conf. Workshop Proc.*, [32, 55](#)
- McCarthy, P. J., van Breugel, W., Spinrad, H., & Djorgovski, S. 1987, *ApJ*, [321, L29](#)
- McNamara, B. R., & Nulsen, P. E. J. 2012, *New J. Phys.*, [14, 055023](#)
- Miley, G. K., Heckman, T. M., Butcher, H. R., & van Breugel, W. J. M. 1981, *ApJ*, [247, L5](#)
- Mukherjee, D., Bicknell, G. V., Wagner, A. Y., Sutherland, R. S., & Silk, J. 2018, *MNRAS*, [479, 5544](#)
- Natarajan, P., & Pringle, J. E. 1998, *ApJ*, [506, L97](#)
- Privon, G. C., O'Dea, C. P., Baum, S. A., et al. 2008, *ApJS*, [175, 423](#)
- Rees, M. J. 1978, *Nature*, [275, 516](#)
- Richstone, D. O., & Oke, J. B. 1977, *ApJ*, [213, 8](#)
- Saxena, A., Röttgering, H. J. A., & Rigby, E. E. 2017, *MNRAS*, [469, 4083](#)
- Scheuer, P. A. G., & Feiler, R. 1996, *MNRAS*, [282, 291](#)
- Serra, P., Oosterloo, T., Morganti, R., et al. 2012, *MNRAS*, [422, 1835](#)
- Singh, R., van de Ven, G., Jahnke, K., et al. 2013, *A&A*, [558, A43](#)
- Solórzano-Iñarrea, C., & Tadhunter, C. N. 2003, *MNRAS*, [340, 705](#)
- Sparks, W. B., Baum, S. A., Biretta, J., Macchetto, F. D., & Martel, A. R. 2000, *ApJ*, [542, 667](#)
- Speranza, G., Balmaverde, B., Capetti, A., et al. 2021, *A&A*, [653, A150](#)
- Spinrad, H., Marr, J., Aguilar, L., & Djorgovski, S. 1985, *PASP*, [97, 932](#)
- Stockton, A. 1976, *ApJ*, [205, L113](#)
- Stockton, A., & MacKenty, J. W. 1983, *Nature*, [305, 678](#)
- Stockton, A., & MacKenty, J. W. 1987, *ApJ*, [316, 584](#)
- Stockton, A., MacKenty, J. W., Hu, E. M., & Kim, T.-S. 2002, *ApJ*, [572, 735](#)
- Stockton, A., Fu, H., & Canalizo, G. 2006, *New Astron. Rev.*, [50, 694](#)
- Tadhunter, C. N., Morganti, R., Robinson, A., et al. 1998, *MNRAS*, [298, 1035](#)
- Tadhunter, C. N., Villar-Martin, M., Morganti, R., Bland-Hawthorn, J., & Axon, D. 2000, *MNRAS*, [314, 849](#)
- Veilleux, S., & Osterbrock, D. E. 1987, *ApJS*, [63, 295](#)
- Wampler, E. J., Robinson, L. B., Burbidge, E. M., & Baldwin, J. A. 1975, *ApJ*, [198, L49](#)

Appendix A: Emission line images and velocity curves

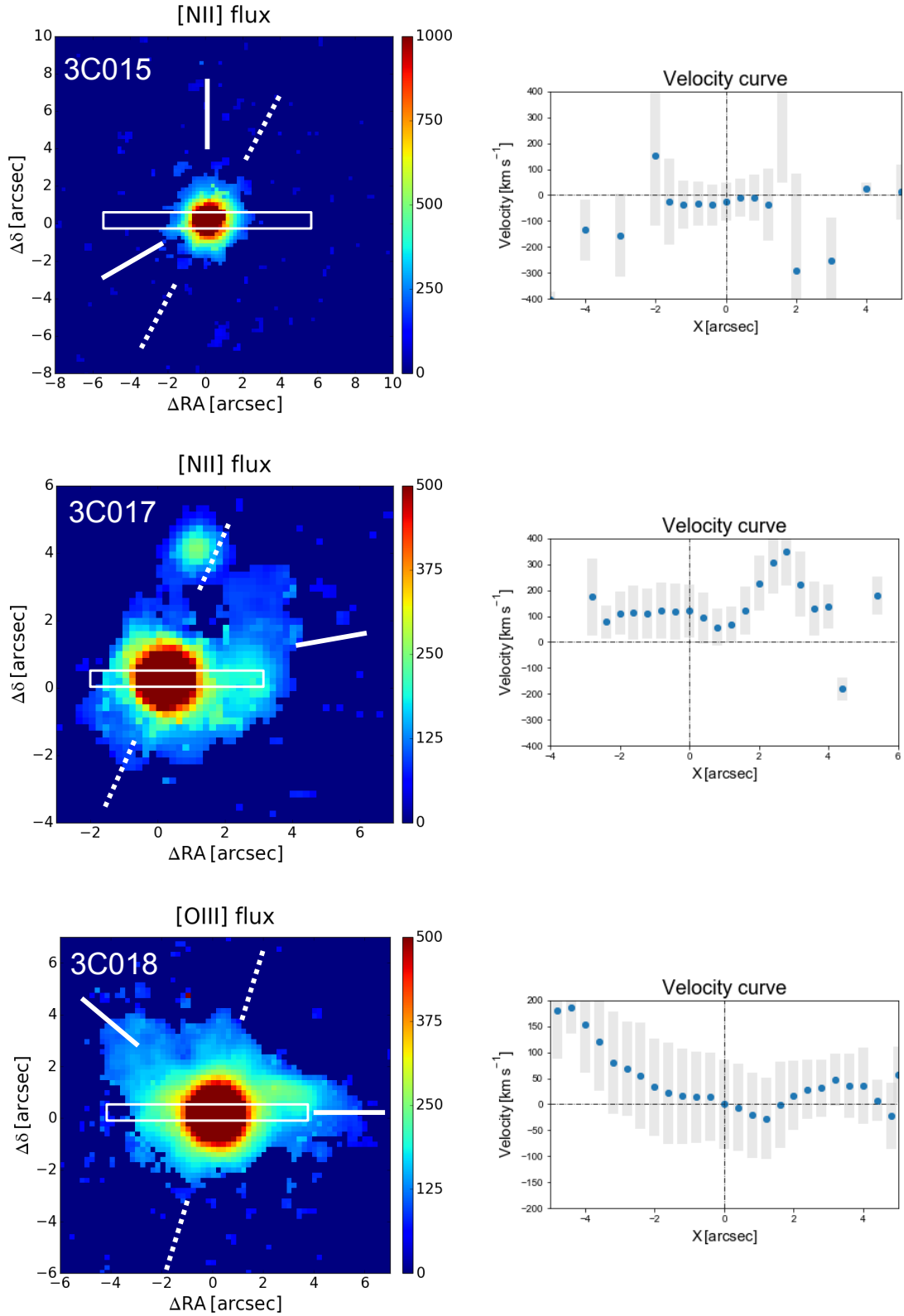


Fig. A.1. Images of the brightest emission line for the 37 radiogalaxies observed with MUSE. The white dotted lines mark the radio position angle, and the solid white lines show the orientation of the emission line structures, when possible, on both sides of the nucleus. The gray line is the orientation of the kinematical major axis in the inner regions measured with kinemetry for all sources with data quality sufficient for a robust measurement (see text for details). The rectangle represents the regions from which we extracted the velocity curve shown in the right panel. The length of the gray bars represents the line width at each location.

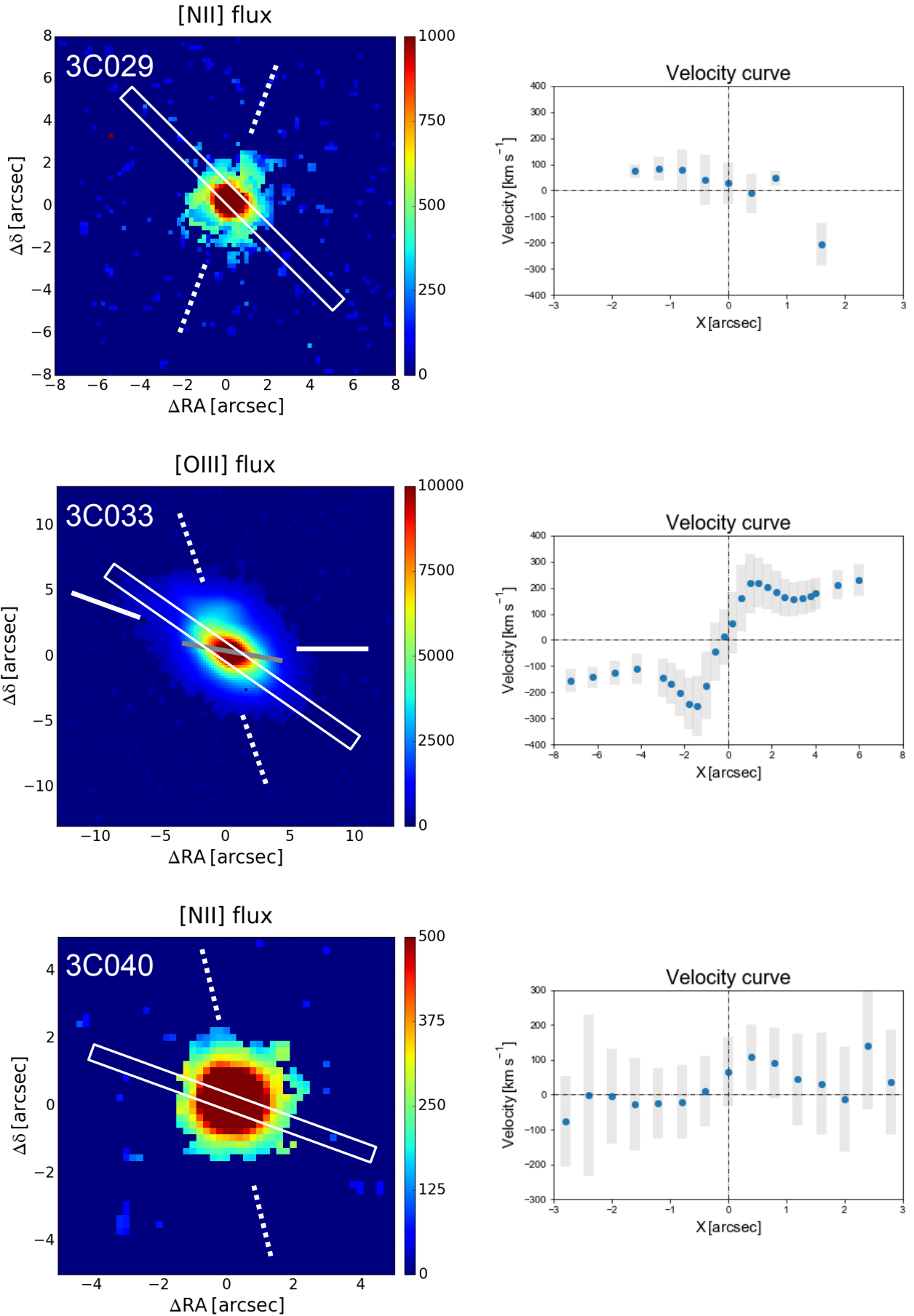


Fig. A.1. continued.

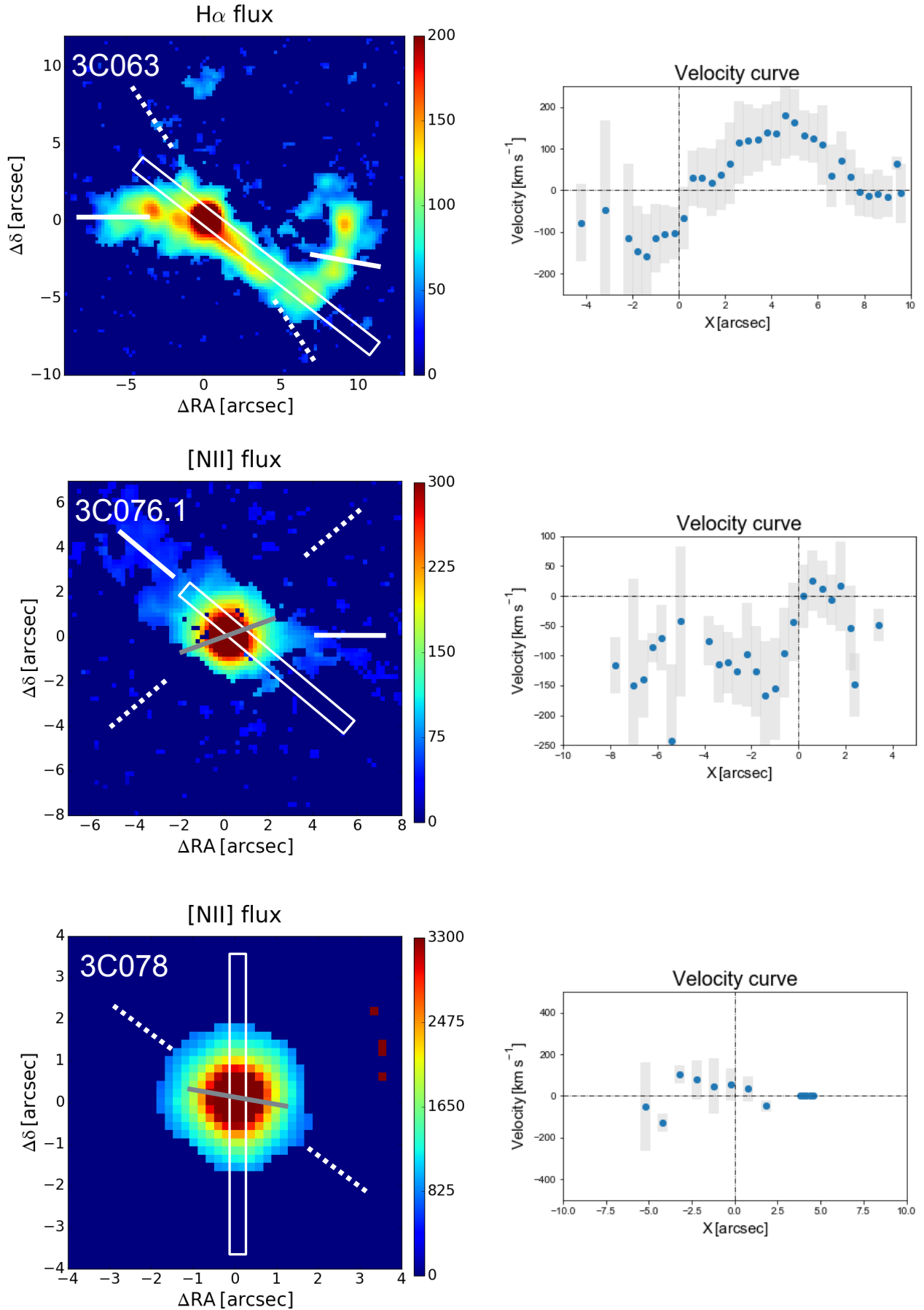


Fig. A.1. continued.

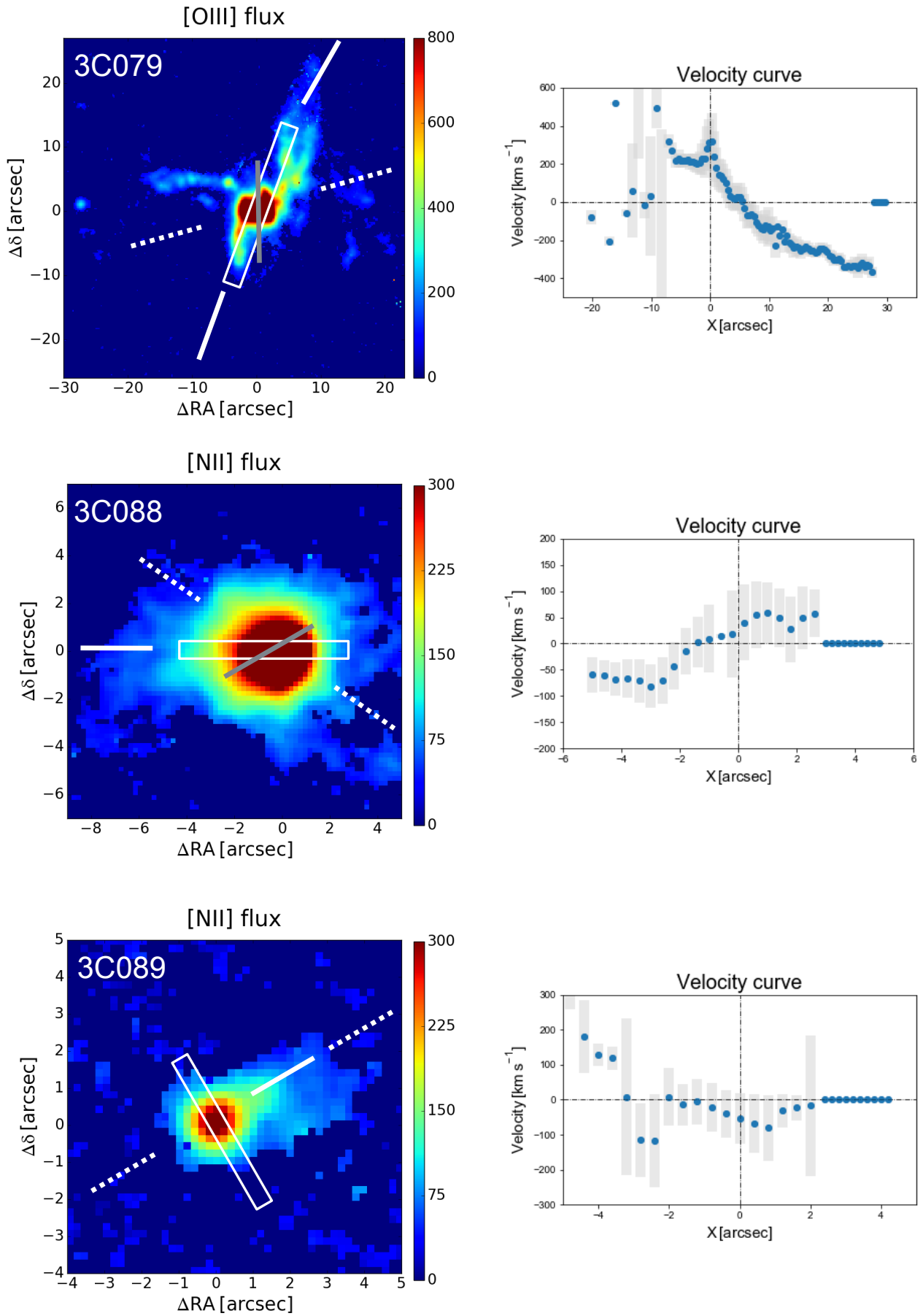


Fig. A.1. continued.

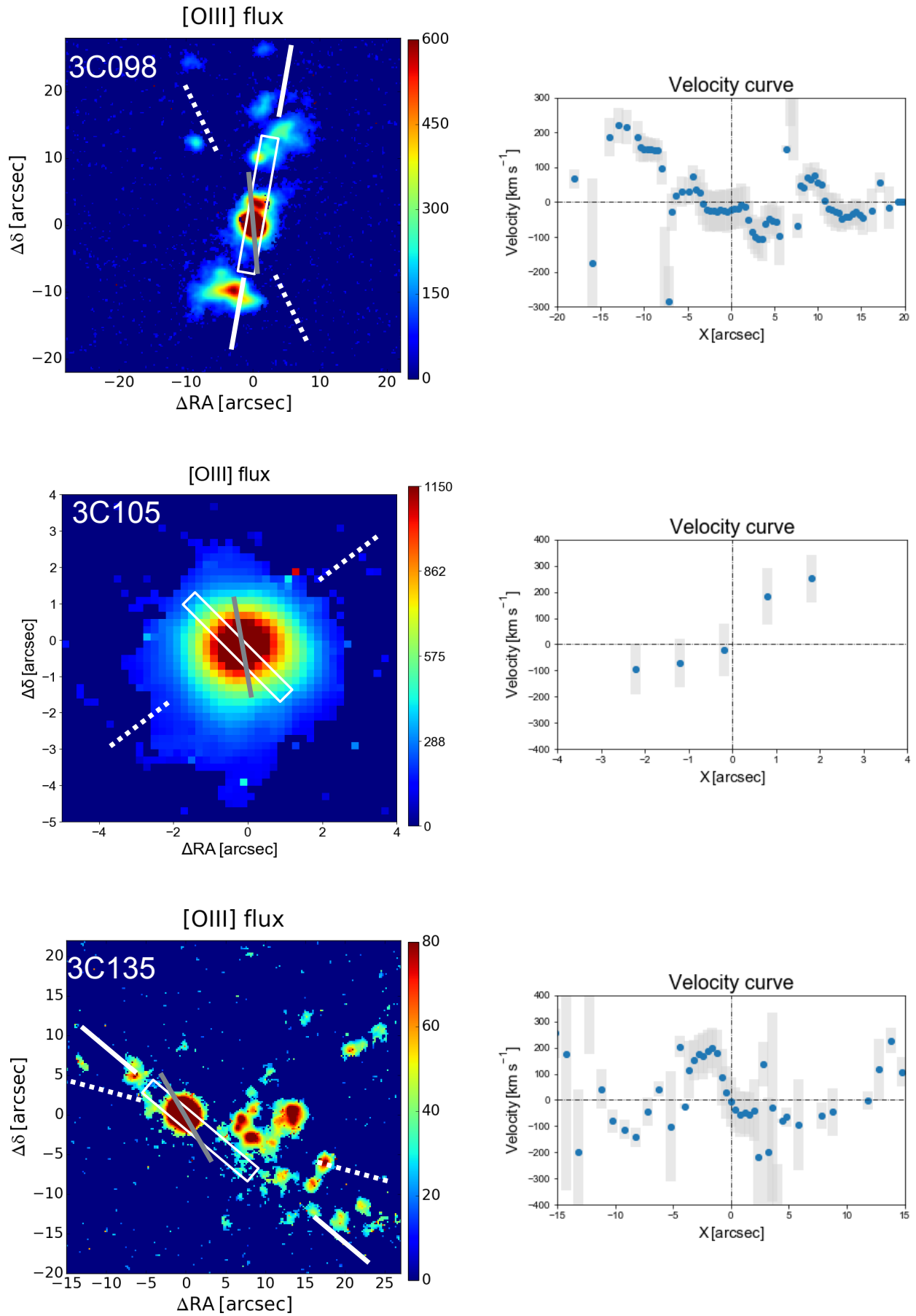


Fig. A.1. continued.

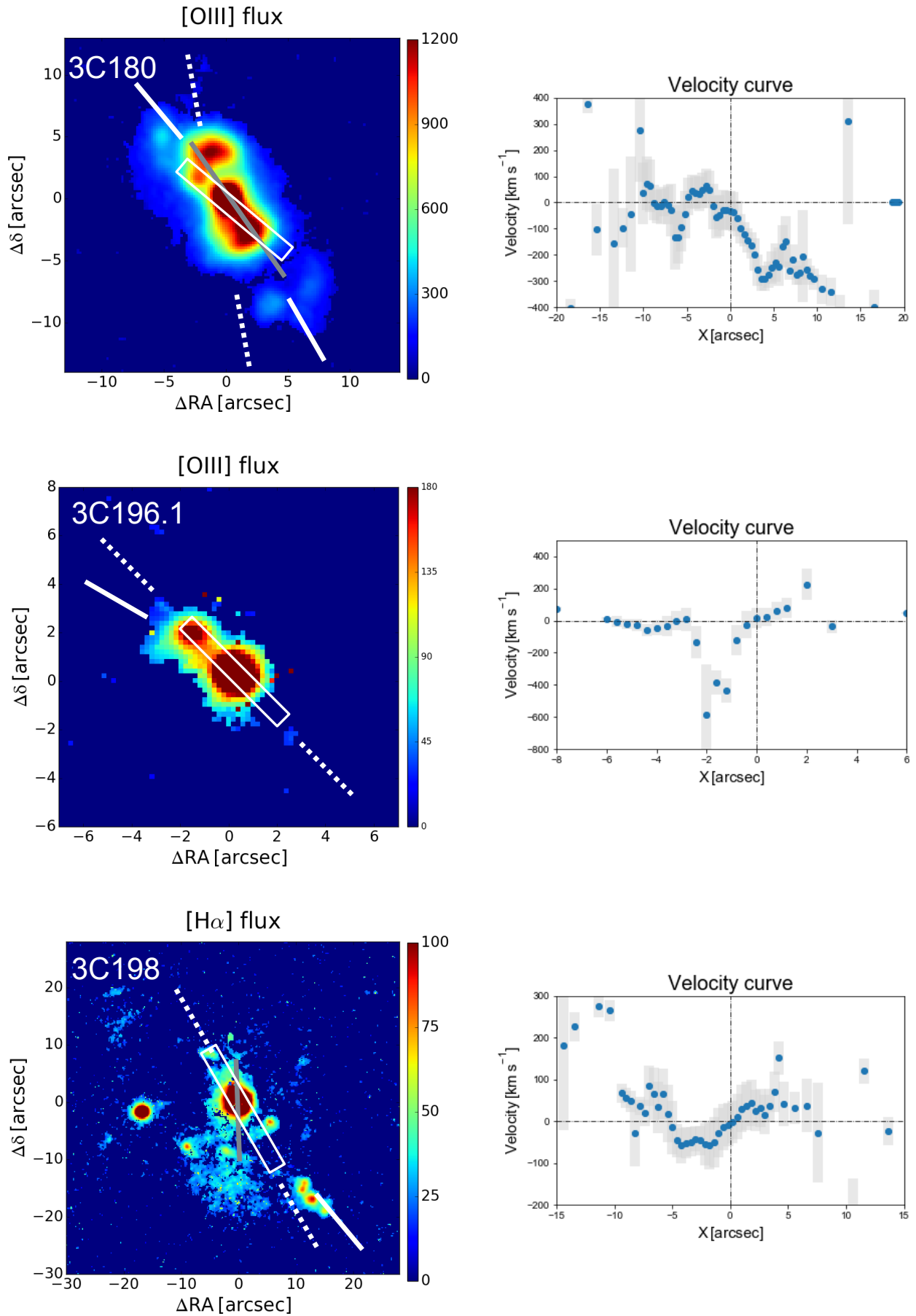


Fig. A.1. continued.

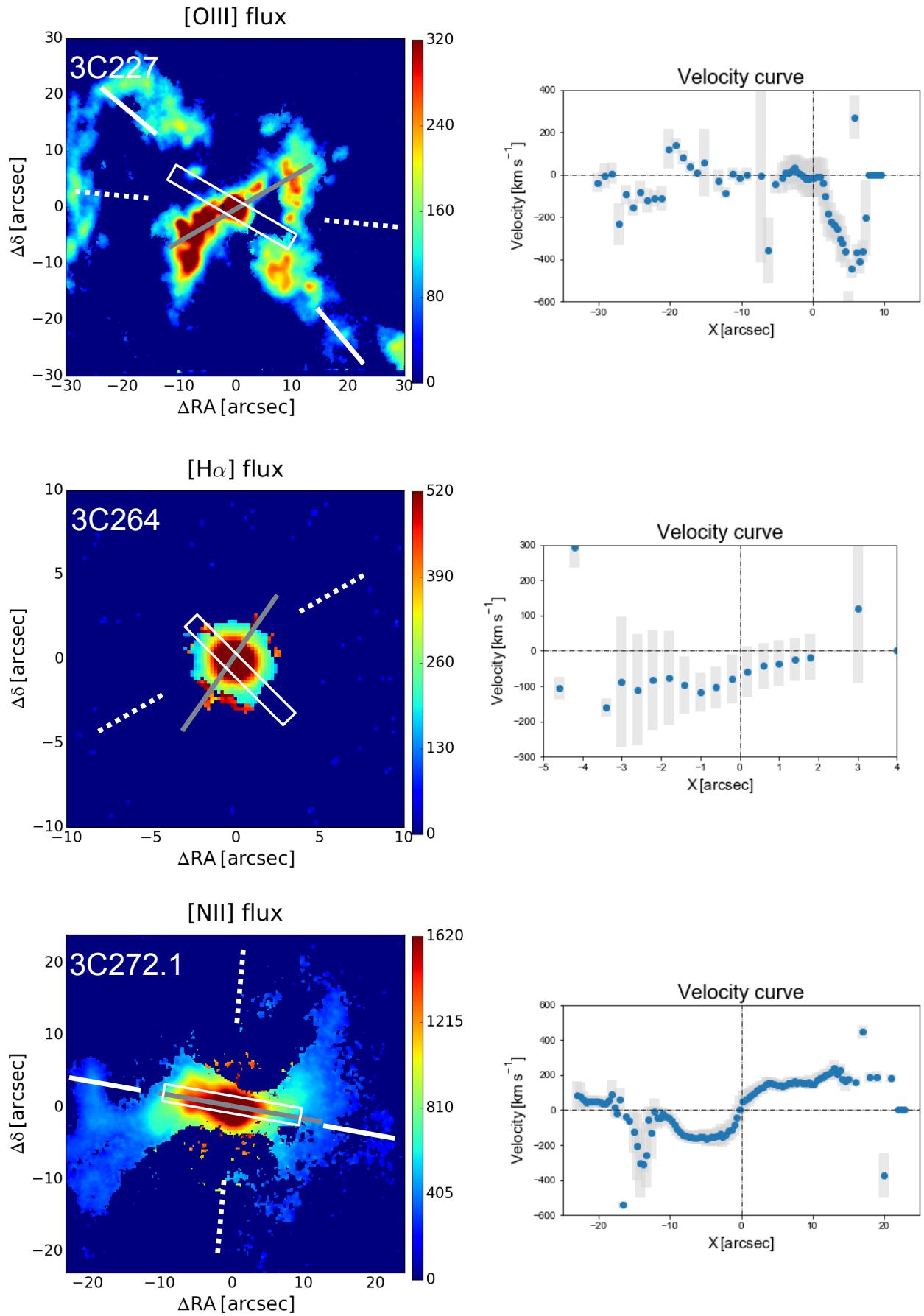


Fig. A.1. continued.

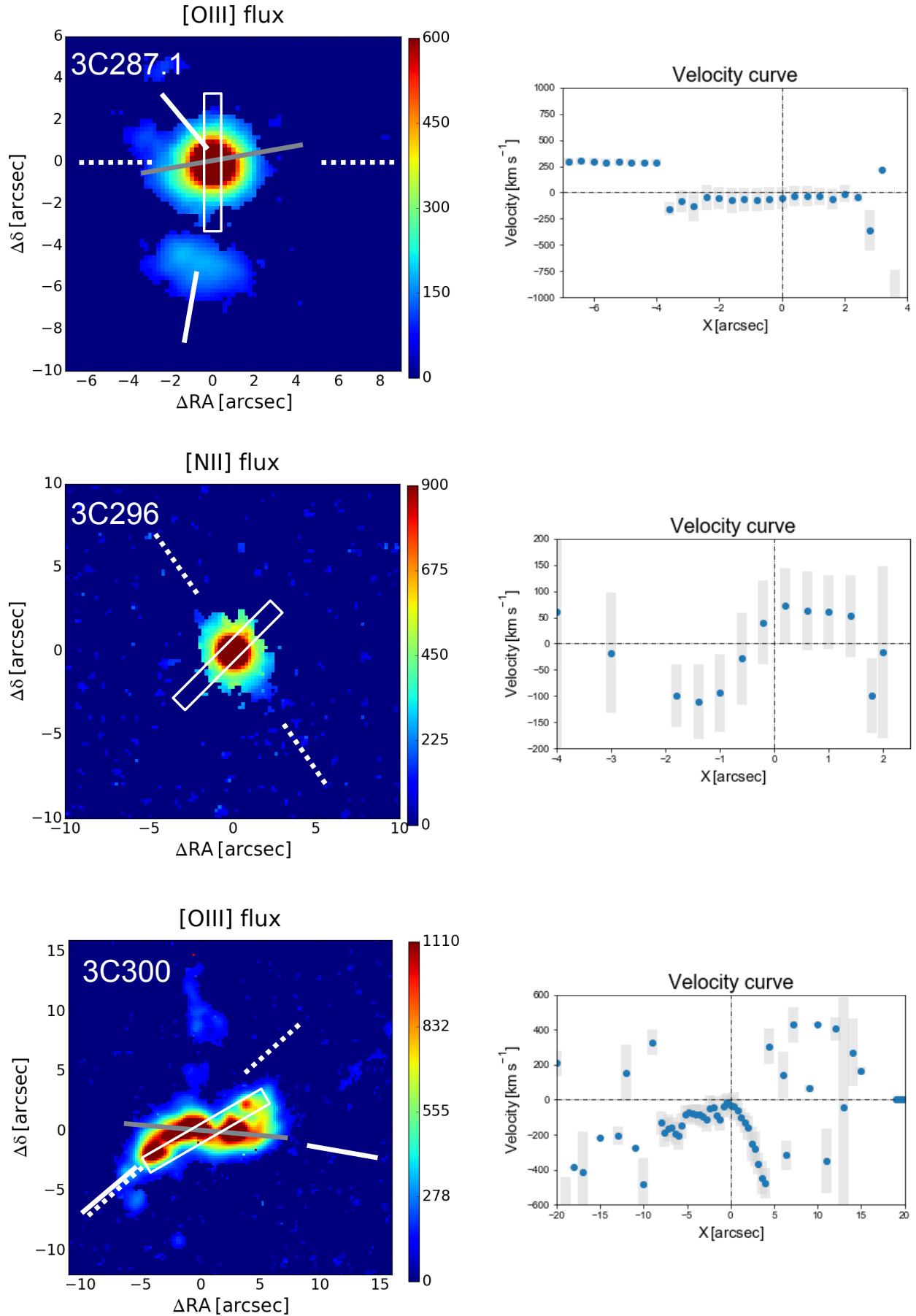


Fig. A.1. continued.

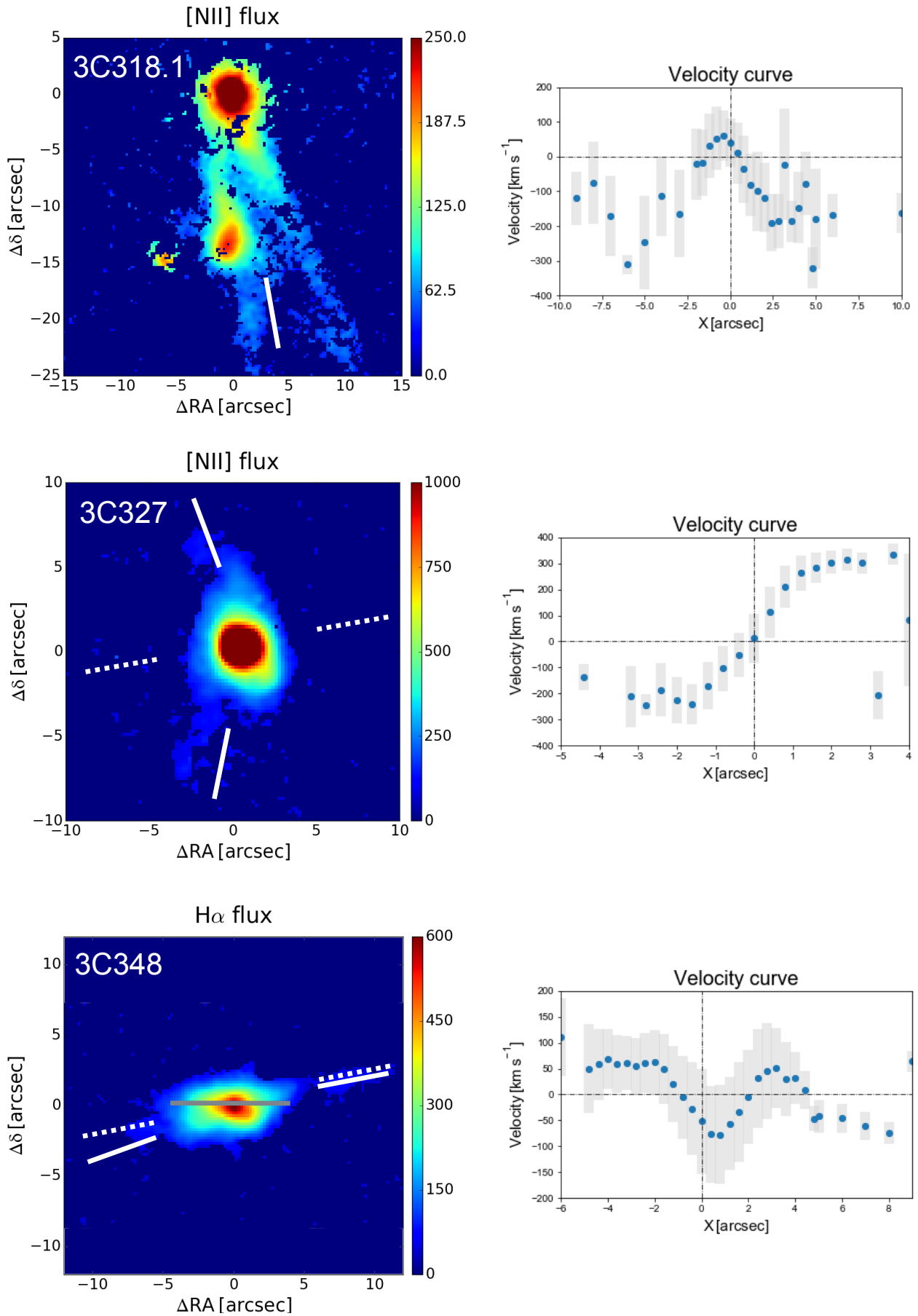


Fig. A.1. continued.

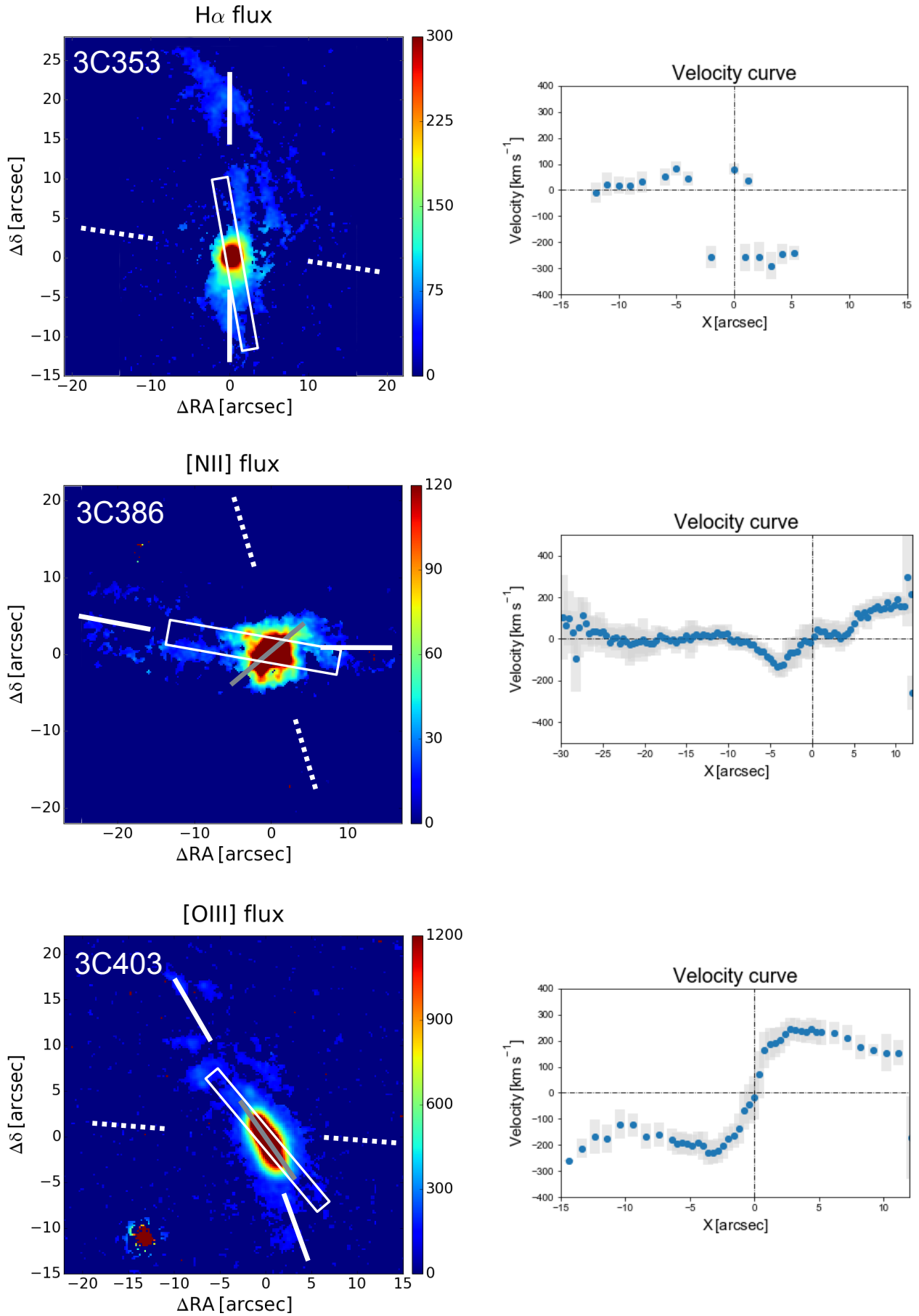


Fig. A.1. continued.

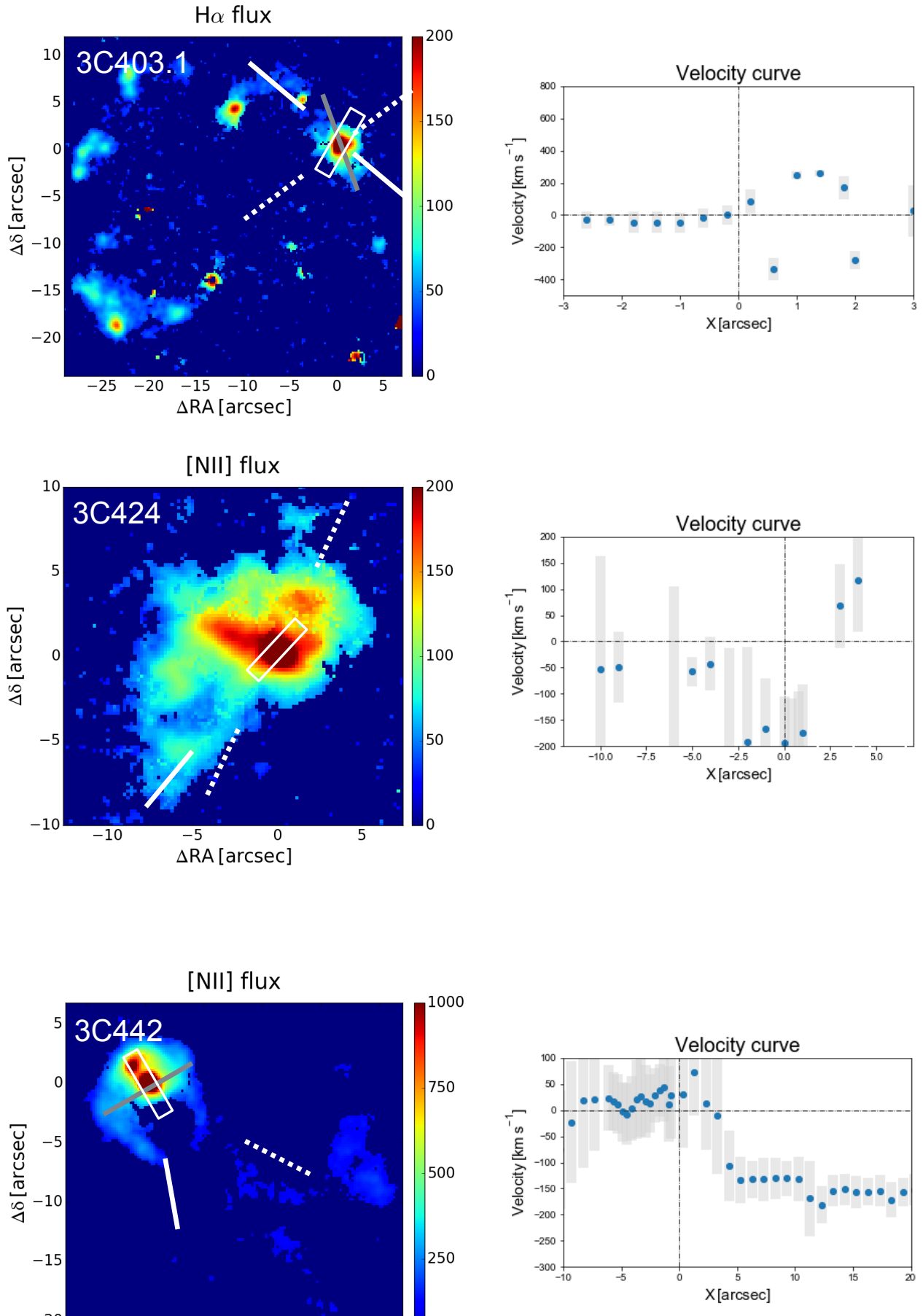


Fig. A.1. continued.

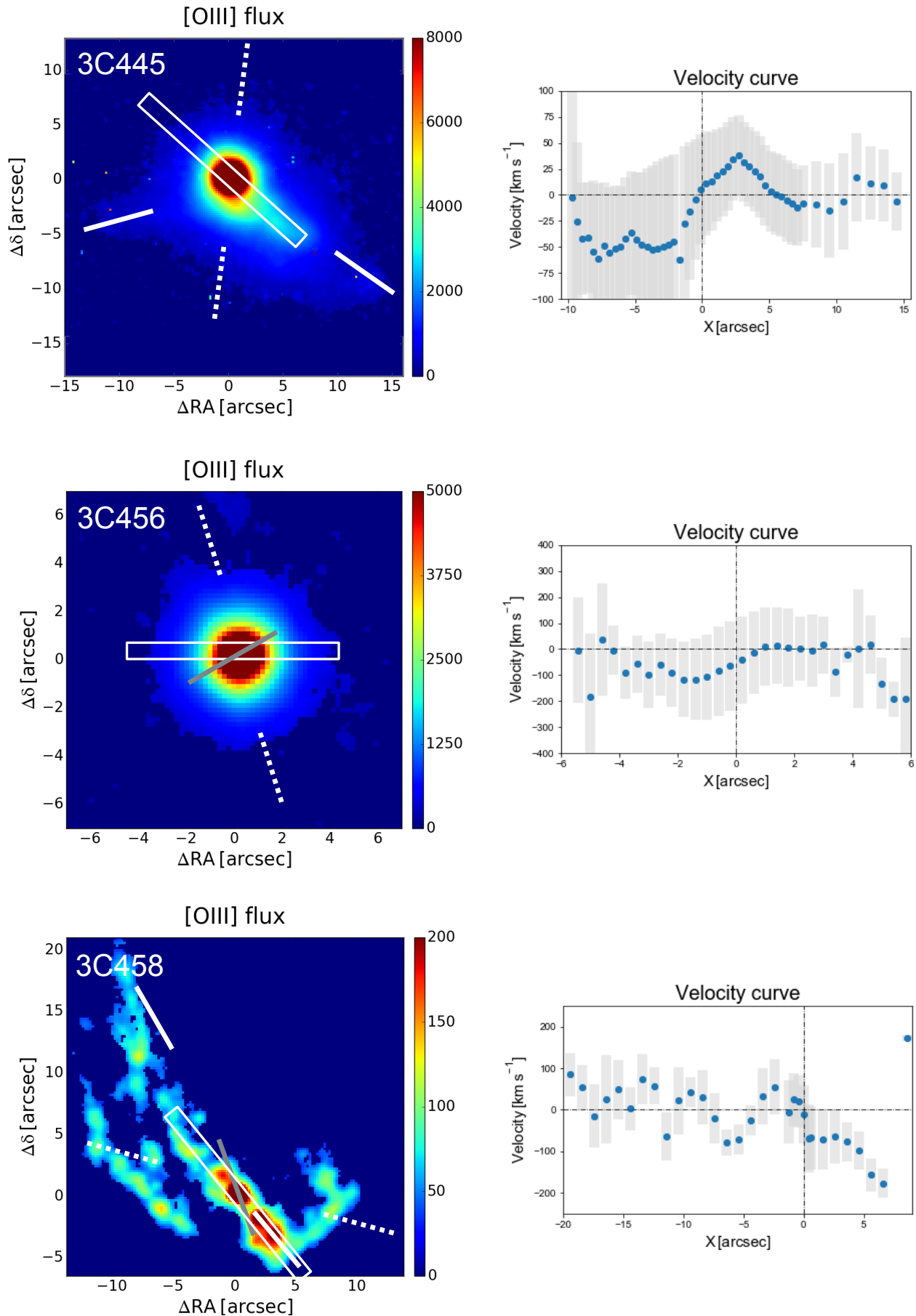


Fig. A.1. continued.

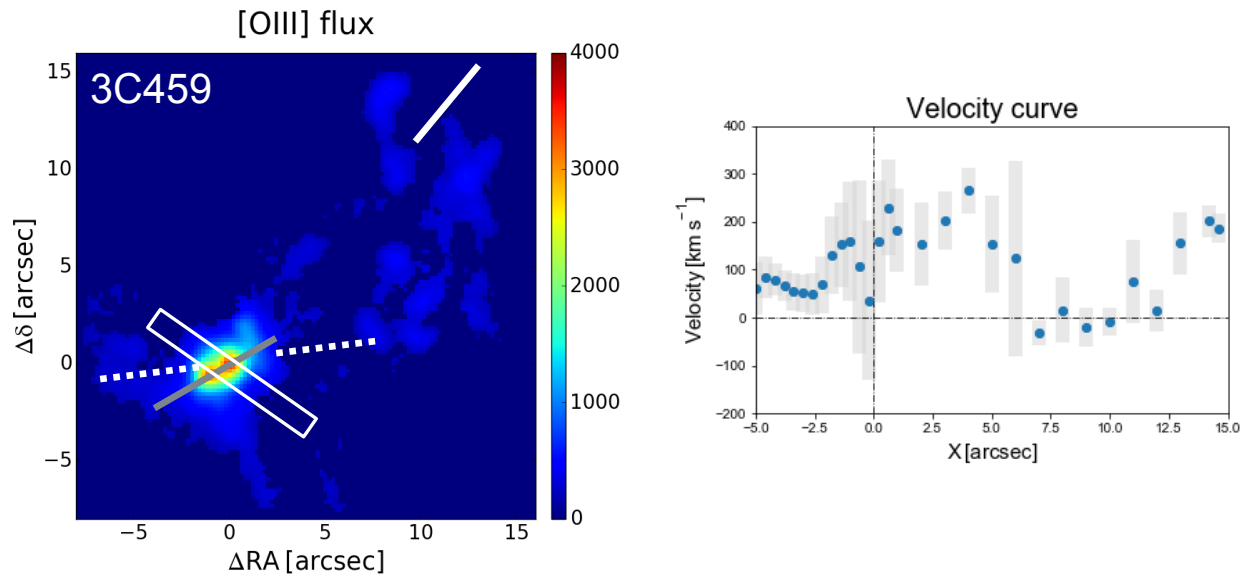


Fig. A.1. continued.

Appendix B: Polar diagrams of the emission lines' distribution

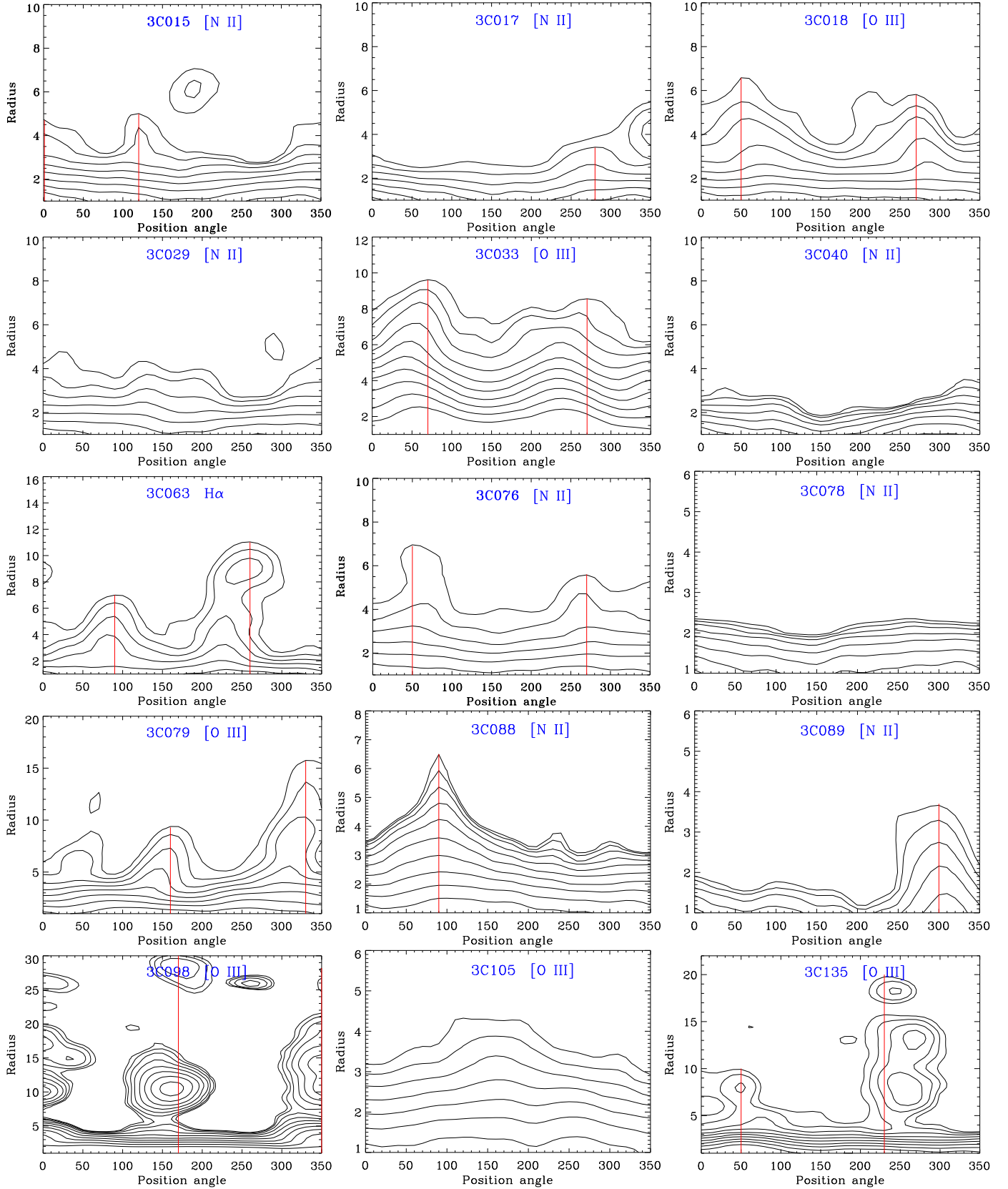


Fig. B.1. Polar diagrams of the emission lines reported in Tab. 1 for all the 3C radio galaxies. The solid red lines mark the ionized gas position angle on each side of the nucleus.

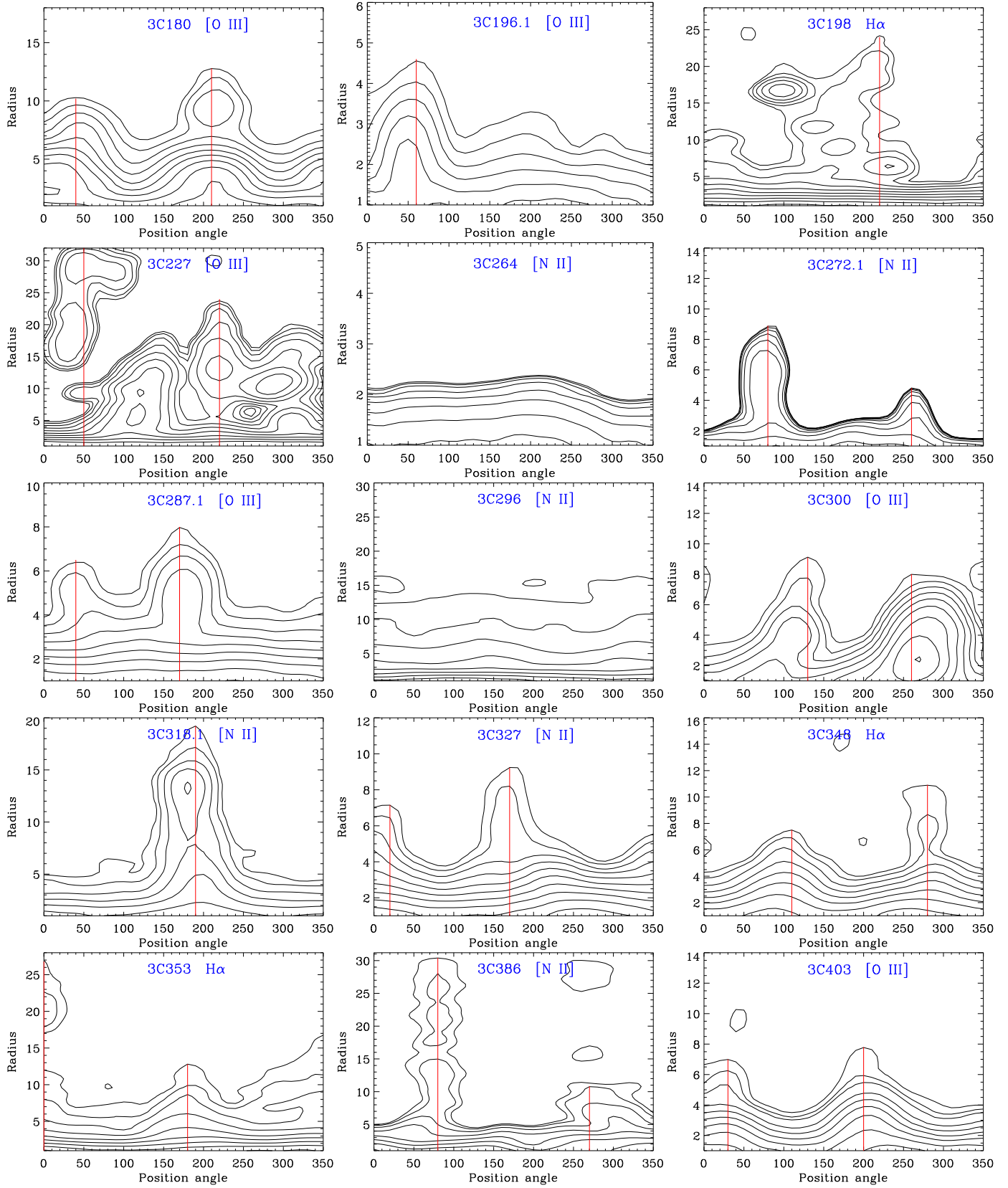


Fig. B.1. continued.

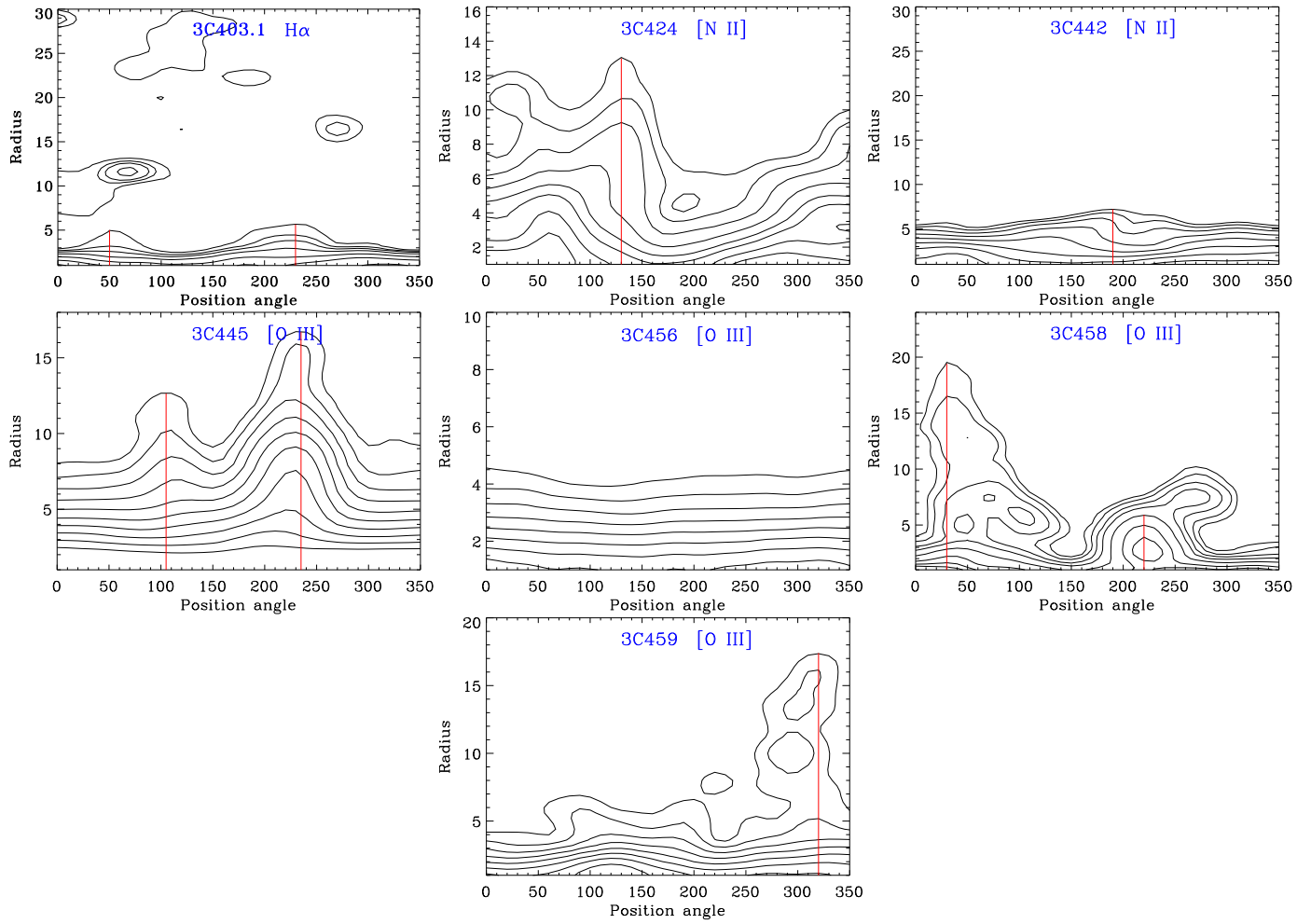


Fig. B.1. continued.

Appendix C: Kinematics of the nuclear gas

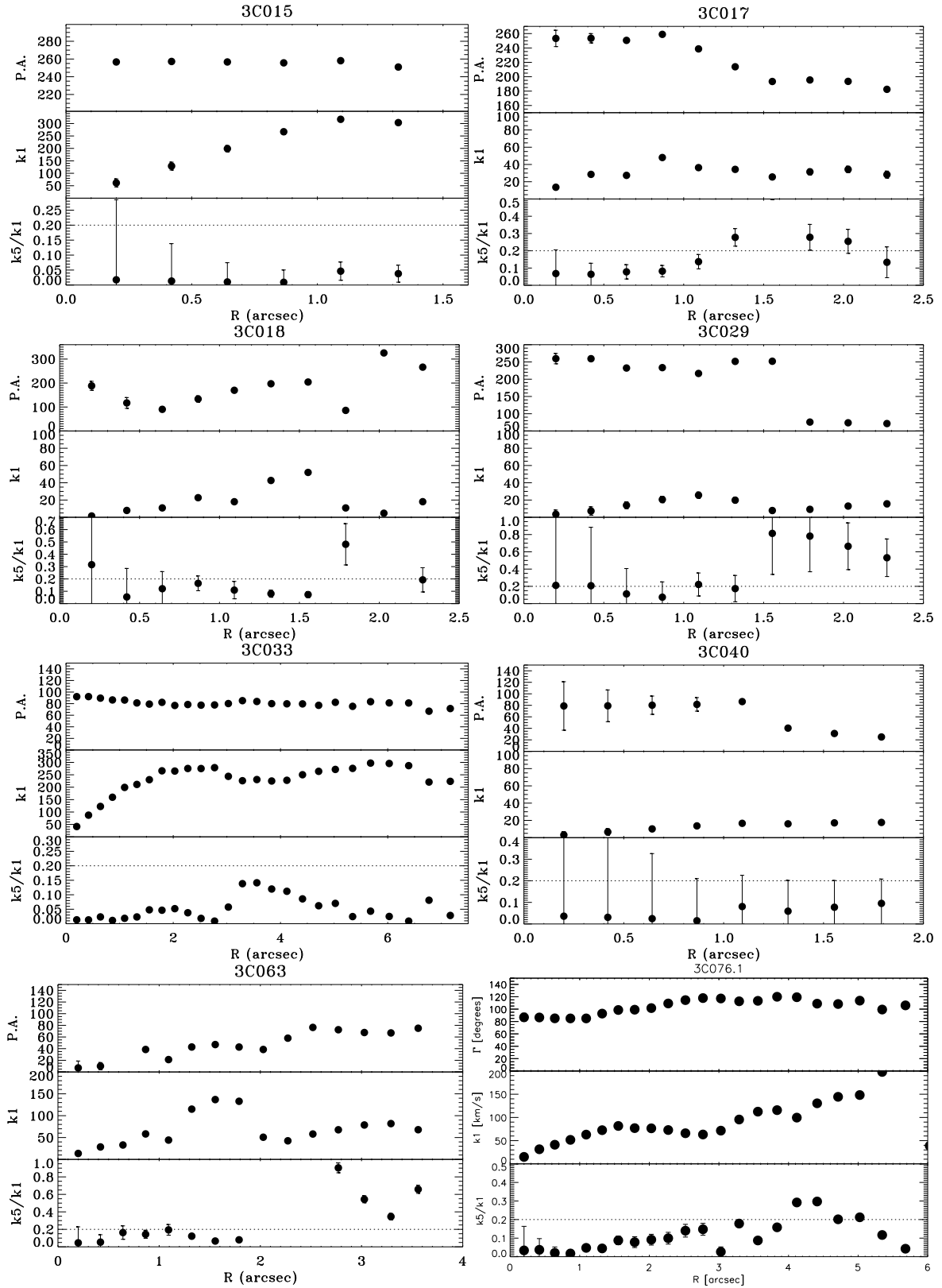


Fig. C.1. Results obtained for 36 radio galaxies (all but 3C 089) with the kinemetry software. From top to bottom in each panel: the kinematic position angle PA (in degrees), the amplitude of the rotation curve (in km s^{-1}), and the ratio between the fifth and first coefficient k_5/k_1 , which quantifies the deviations from simple rotation.

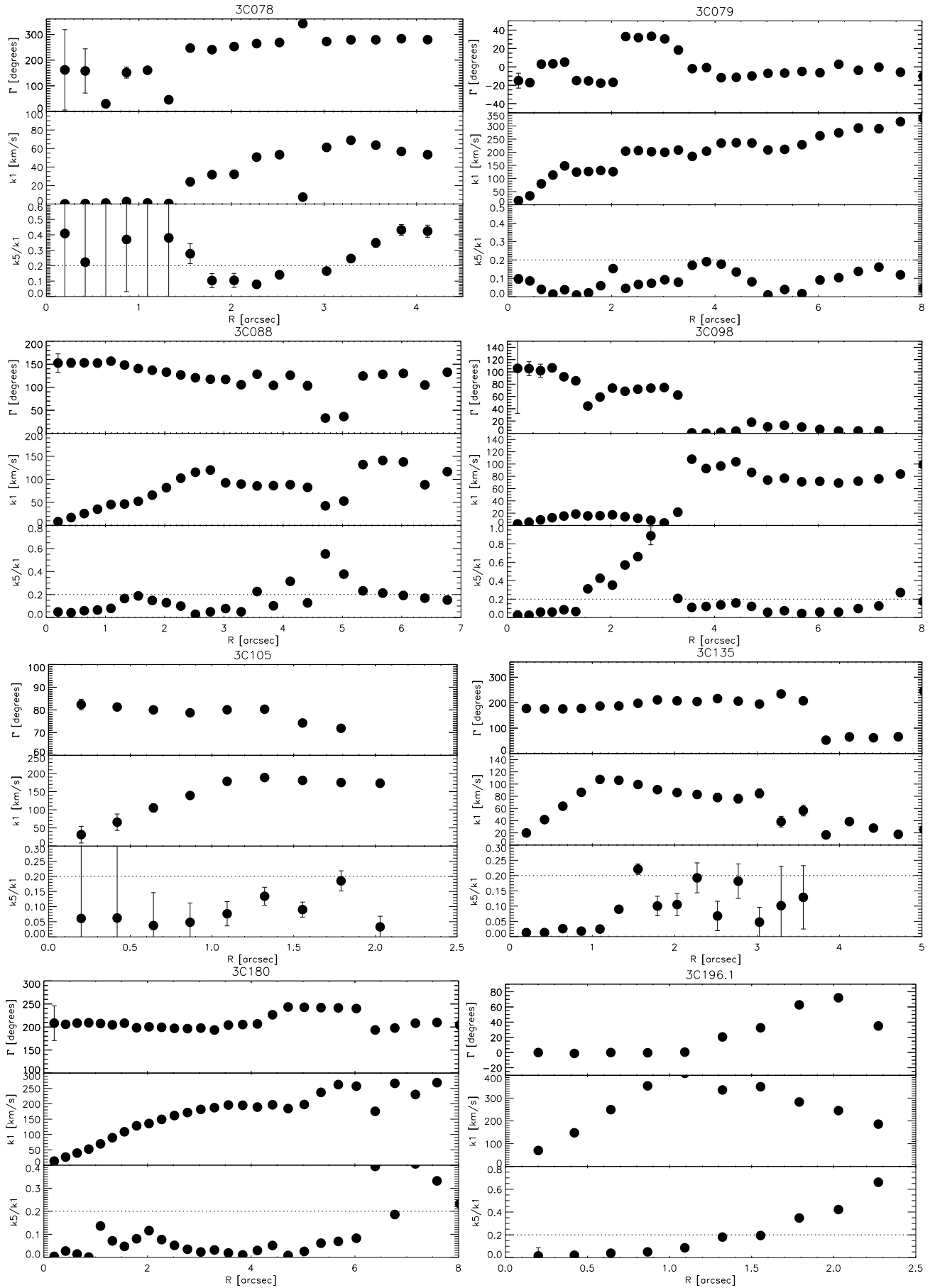


Fig. C.1. continued.

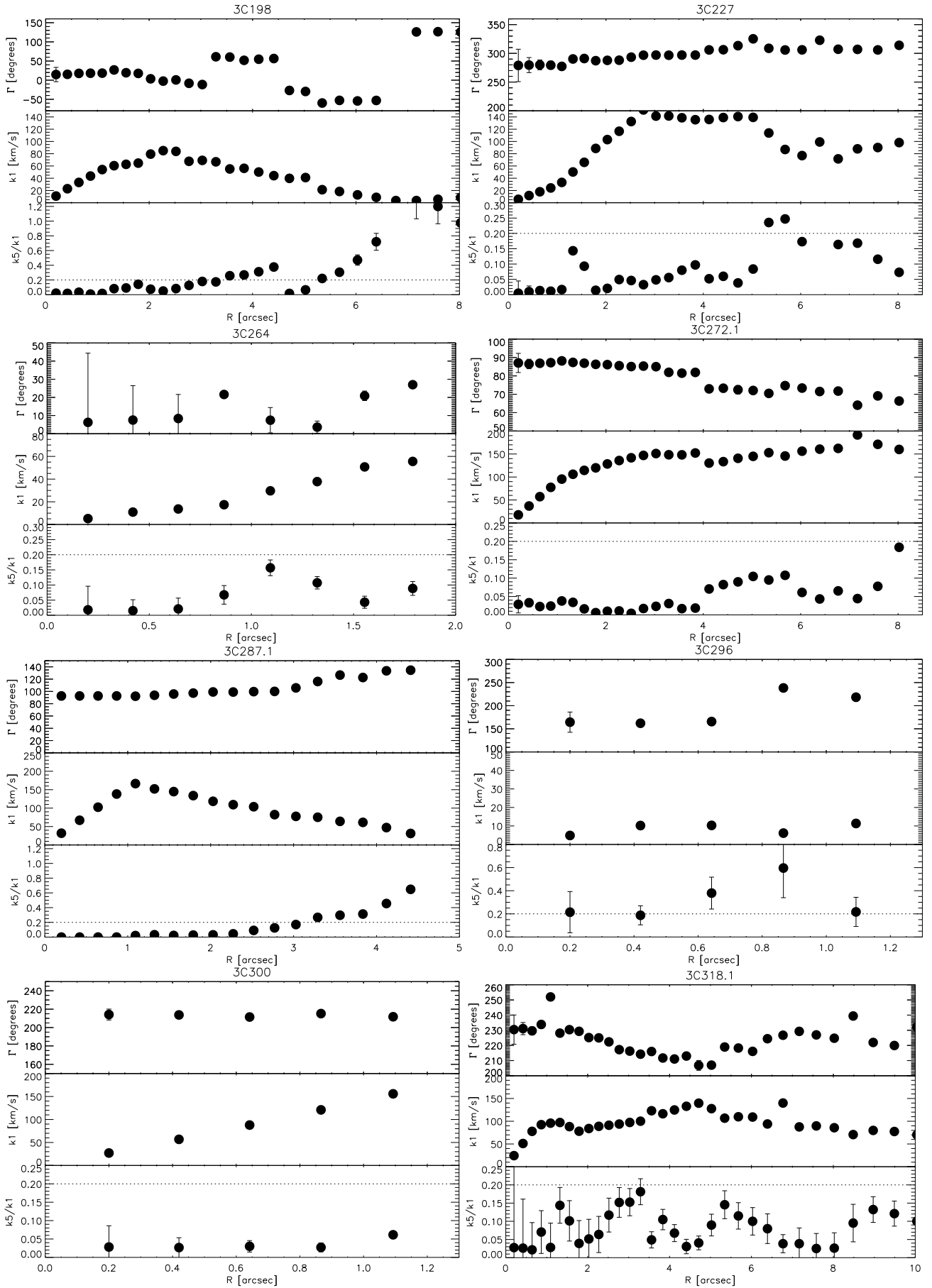


Fig. C.1. continued.

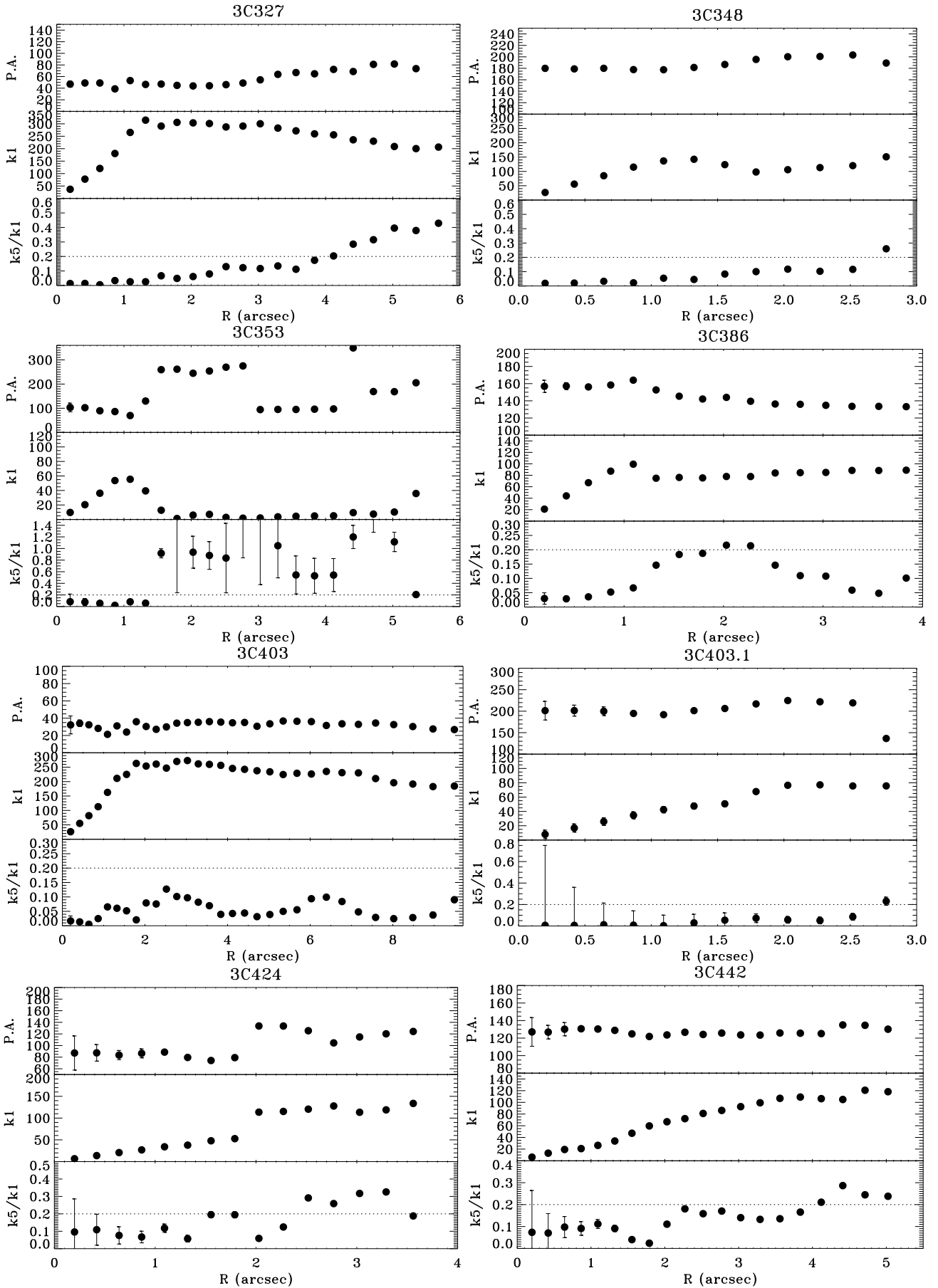


Fig. C.1. continued.

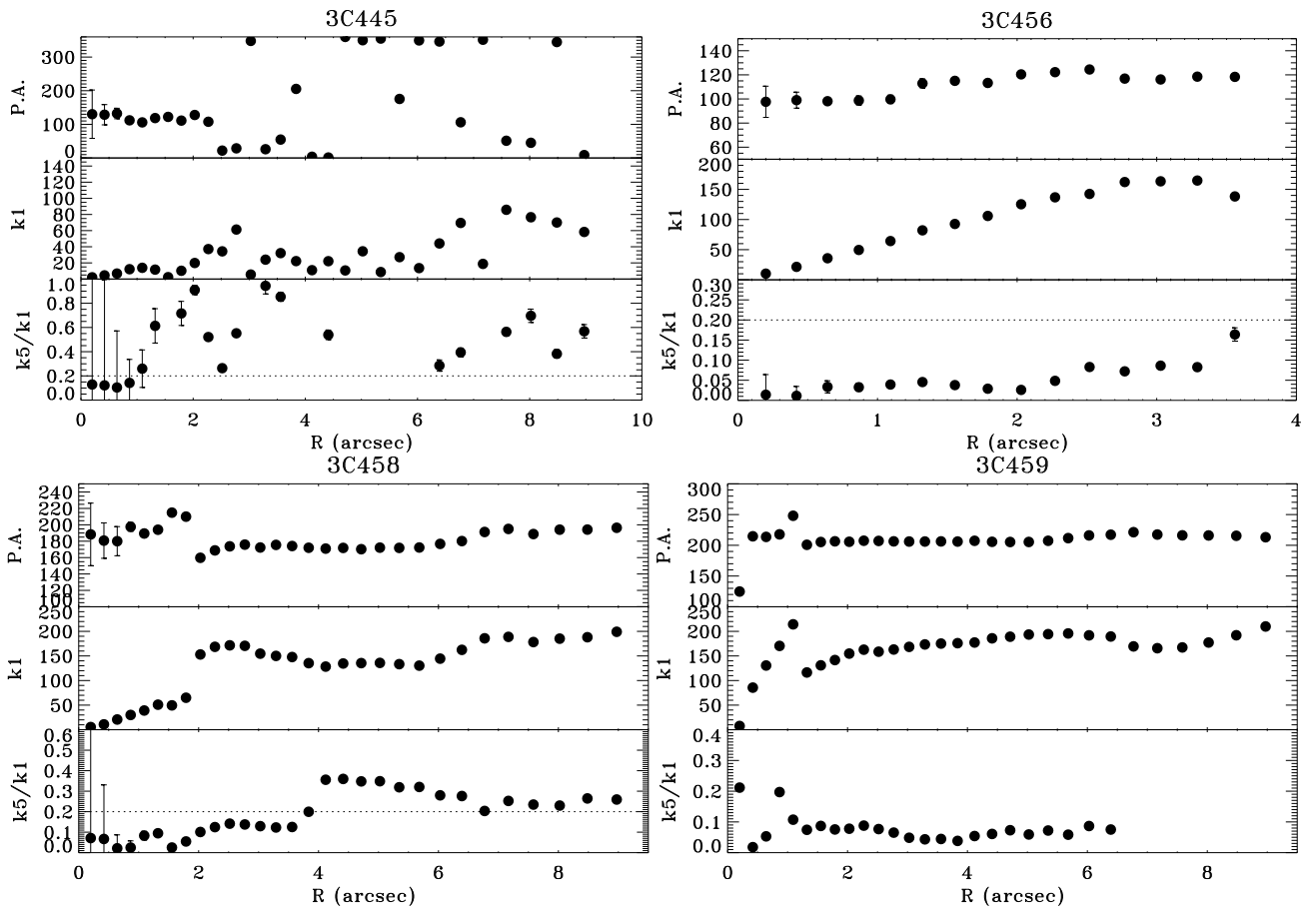


Fig. C.1. continued.

Appendix D: Superposition of radio contours onto the emission line images

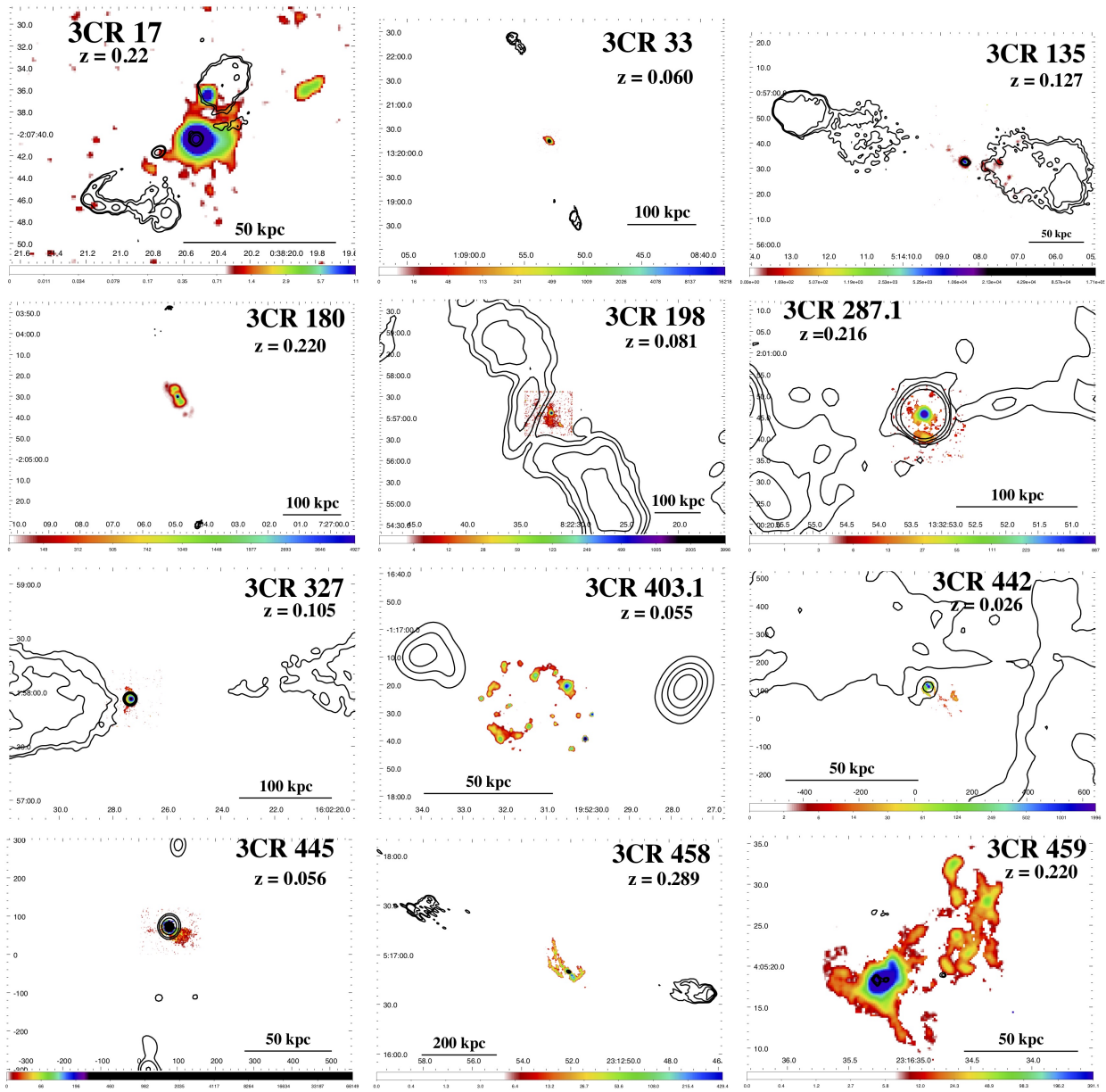


Fig. D.1. Superposition of the radio contours onto the gas velocity maps for the sources with extended emission line regions not already shown in Fig. 5.

Appendix E: Offnuclear spectra

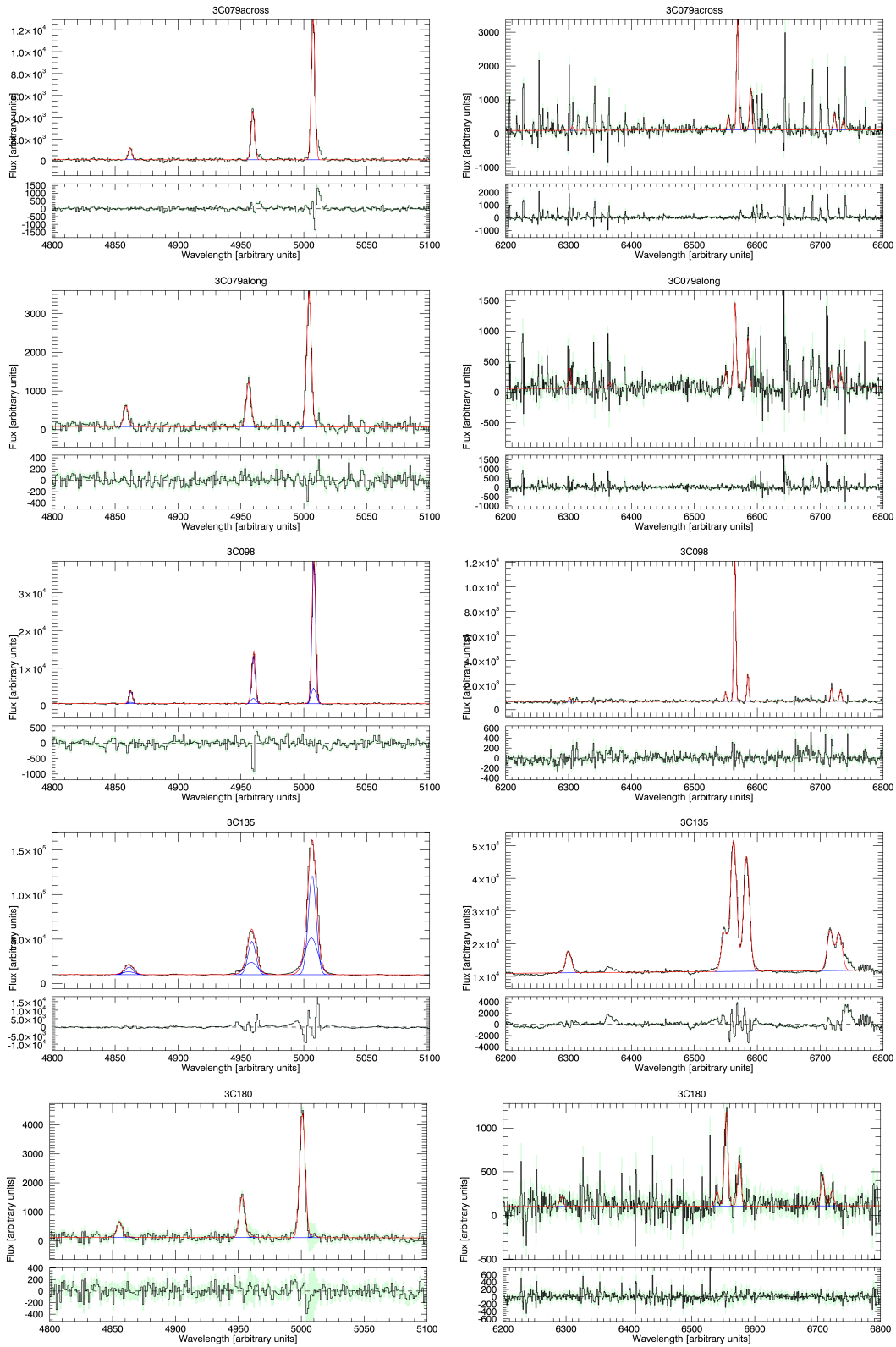


Fig. E.1. Off-nuclear spectra of the sources for which it was possible to obtain this information. The blue portion of the spectra are on the left side, and the red portion of spectra are on the right side. The spectra are in black, and the emission line fit is in red (when two components are required, they are shown separately in blue). The gray areas represent the errors in the spectra. The bottom panels show the residuals.

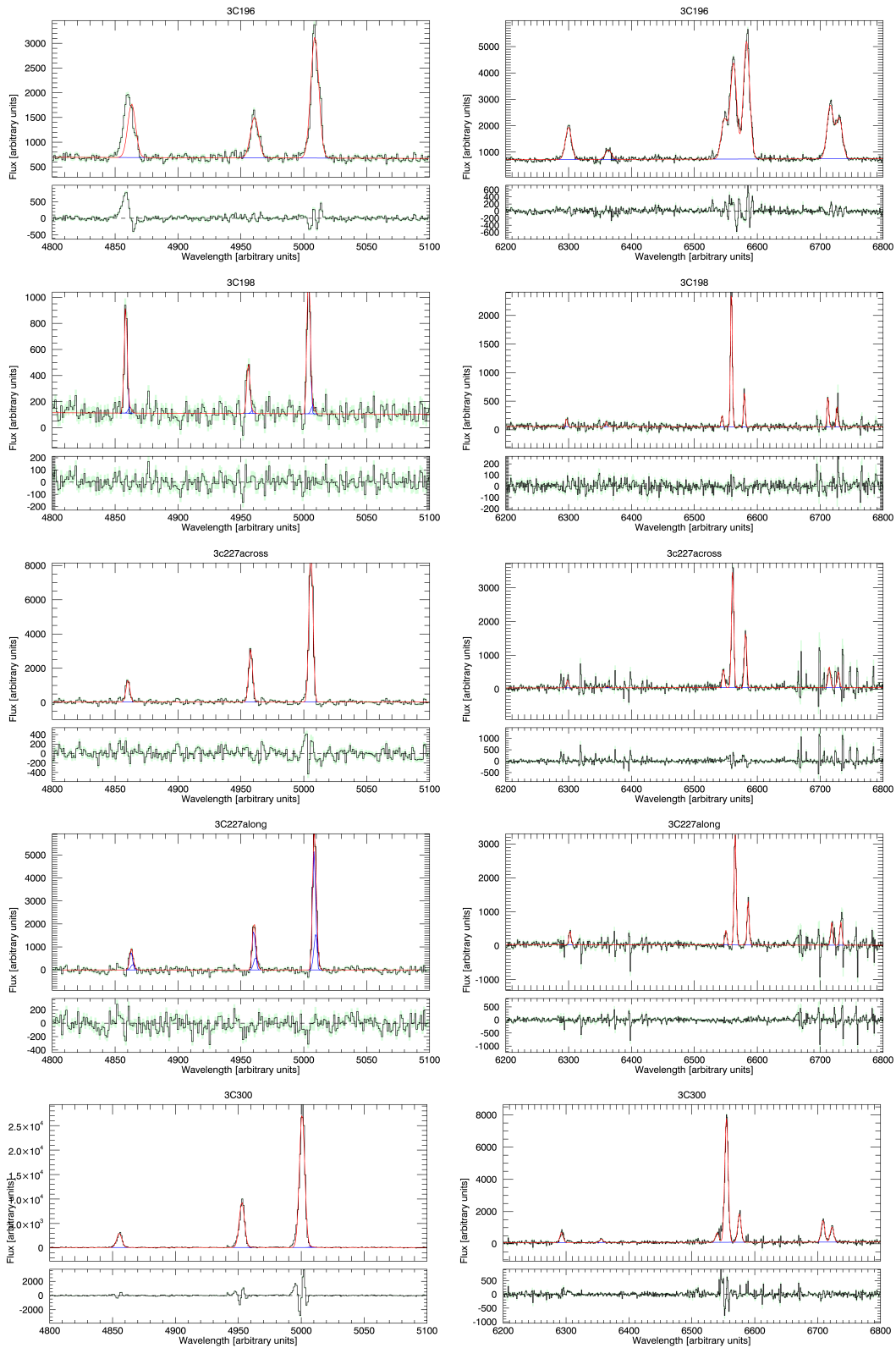


Fig. E.1. continued.